National Technical University of Athens

Naval and Marine Technology Master Program

Offshore Structures Section

School of Naval Architecture and Marine Engineering

Hydrodynamic Analysis of a Porous Cylindrical Body

Master Thesis

Boufidi Ifigeneia

Supervisor
Professor: Ioannis K. Chatjigeorgiou

Athens, 2022

Acknowledgments

First and foremost, I would like to express my gratitude to my supervisor, Professor Ioannis K. Chatjigeorgiou who gave me the opportunity for collaboration in such an interesting project. The remarks and the advice he gave me were always very helpful and enlightening.

I would also like to thank Assistant Professor Dimitris Konispoliatis for always being willing to provide help and knowledge. His guidance is what made this project possible.

Last but not least, I would like to thank my family and my friends for every kind of support they provide.

National Technical University of Athens

Naval and Marine Technology Master Program

Offshore Structures Section

School of Naval Architecture and Marine Engineering

Hydrodynamic Analysis of a Porous Cylindrical Body

Master Thesis

Boufidi Ifigeneia

Supervisor
Professor: Ioannis K. Chatjigeorgiou

Athens, 2022

Abstract

In this study, the problems of diffraction and radiation of water waves from a surface porous cylindrical body are considered. The body is free floating in a constant water depth, and is consisted of a porous sidewall and impermeable bottom. Within the realms of linear potential theory, a three dimensional solution based on the method of matched eigenfunction expansions is applied in order to predict the velocity potential of the flow field surround the body. Numerical results are presented and discussed concerning the effect the porosity, the draught and the radius have on the cylindrical body's hydrodynamic forces and moments. It is revealed by the results that the porosity and the dimensions of the body play a significant role in either reducing or increasing the exciting wave loads.

Εθνικό Μετσόβιο Πολυτεχνείο

Δ.Π.Μ.Σ Ναυτική και Θαλάσσια Τεχνολογία

Κατεύθυνση: Θαλάσσιες Κατασκευές και Εκμετάλλευση Υδρογονανθράκων

Σχολή Ναυπηγών Μηχανολόγων Μηχανικών

Υδροδυναμική Ανάλυση Διάτρητου Κυλινδρικού Σώματος

Μεταπτυχιακή Εργασία

Μπουφίδη Ιφιγένεια

Επιβλέπων
Καθηγητής: Ιωάννης Κ. Χατζηγεωργίου

Αθήνα, 2022

Περίληψη

Στην παρούσα μελέτη εξετάζονται τα προβλήματα της διάθλασης και ακτινοβολίας κυματισμών, από την παρουσία πορώδους κυλινδρικού σώματος. Το σώμα πλέει ελεύθερο σε σταθερό βάθος, διαπερνά την ελεύθερη επιφάνεια και αποτελείται από διάτρητη εξωτερική επιφάνεια και αδιαπερατό πυθμένα. Στα πλαίσια της γραμμικής θεωρίας κυματισμών, εφαρμόστηκε τρισδιάστατη μέθοδος ανάπτυξης ιδιοσυναρτήσεων ώστε να υπολογιστεί το δυναμικό ταχύτητας του πεδίου ροής που περιβάλλει το σώμα. Στην συνέχεια, παρουσιάζονται και σχολιάζονται αριθμητικά αποτελέσματα που αφορούν την επίδραση του πορώδους, της ακτίνας και του βυθίσματος του διάτρητου κυλινδρικού σώματος στα υδροδυναμικά φορτία. Γίνεται εμφανές, οτι τόσο το πορώδες όσο και οι διαστάσεις του σώματος παίζουν σημαντικό ρόλο στην μείωση ή αυξησή των φορτίων.

Contents

1 Introduction

1.1 Perforated Structures in Offshore Engineering

Perforated structures are commonly used in a variety of applications in offshore engineering. One of the most common uses is the construction of perforated breakwaters and seawalls. The way in which the porosity of these breakwaters dissipates wave energy and reduces wave loads has been thoroughly studied in the literature, as discussed in section (1.2), making them a very suitable choice for protecting coasts and infrastructure. Some typical examples of perforated breakwaters and seawalls are shown in the following figures:

Figure 1.1: Wolnae fishing port of Busan [1]

Figure 1.2: Chilam fishing port of Busan [1]

Figure 1.3: A bottom-sitting, surface-piercing pile breakwater along the coast of Singapore [2]

In Figures [1.1]-[1.2] the type of breakwater (or seawall) depicted is the one first studied by Jarlan [3] and now it bears his name. In fact, they are partially or fully perforated-wall caisson breakwaters. In their simplest form, they consist of a perforated front wall, in the cases depicted Figures [1.1]-[1.2] circular perforated caisson wall, and a vertical impermeable back-wall.

Whereas, in Figure [1.3] the perforated breakwater has no impermeable back-wall. This type of breakwater is particular useful in applications where the wave circulation is of essence. This could be the case, in near-shore applications, e.g harbours or marinas, where it is important to keep the water of being stagnant. Furthermore, the natural wave circulation that is allowed in this type of structures can help improve the water quality and maintain a healthy ecosystem. Additional advantages of this type of perforated breakwater, are the sediment transport along them and the low construction costs when the water is relatively deep [4].

Another important application of perforated/porous structures in offshore engineering is the use of fish cages. The high environmental impact of aquaculture in near-shore applications, and as the availability of coastal areas becomes progressively more limited, the need for offshore aquaculture has become more urgent. In the following Figures [1.4],[1.5] some examples of offshore aquaculture with the use of fish cages are shown:

2

Figure 1.4: Fish cages in Velfjorden, Brønnøy, Norway.

Figure 1.5: The Samkna offshore fish farm site off the Qatar coast in the Persian Gulf.

1.2 Literature Review

The subject of modelling wave interaction with porous structures have been widely studied in the literature through different approaches. In [5]- [6] the Computational Fluid Dynamics (CFD) approach is followed. In this approach, the flow through the porous surface is modelled explicitly. This requires a numerical grid which solves both the small-scale characteristics of the openings in the porous surface and the large scales required for the wave propagation, resulting in a high number of grid cells and correspondingly high computational times. As an alternative, and in order to solve flow fields complex structures, numerical approaches such as Boundary Element Methods (BEM) are required. A few examples of BEM models for wave interaction with porous bodies are [7]- [8]. For less complex structures such as cylinders, plates and vertical barriers (e.g breakwaters), the potential flow methods based on linear wave theory are often preferred. In such approaches, the flow through the porous surface openings is not explicitly modelled, but is rather parameterised on the grounds of the pressure drop as a function of the flow velocity, with a linear or quadratic pressure-velocity relationship.

As aforementioned, the most common use of porous structures on offshore engineering is the use of porous breakwaters. [9]- [10] are just a few, that investigated the wave reflection, transmission and energy dissipation inside such structures, with the application of eigenfunction expansions in the flow field in front and inside the porous medium, as well as behind the breakwater. Using the same method, [11] proved that the wave loads on a semi-porous cylindrical breakwater were significantly reduced due to its porosity. Several subsequent studies followed, which theoretically and experimentally examined the induced wave flow in a porous breakwater and its ability to scatter wave energy and minimize the environmental impact [12]- [13]. In addition, porous plates or meshes are sometimes used to absorb waves in narrow channels [14]- [15] and have have also been studied in the literature because of their ability to freely exchange water or marine species. More specifically,in [16]- [17] in order to analyse small amplitude surface waves generated by a porous plate oscillations, a porous wavemaker theory was developed. While, in [18] the reflection and transmission of small amplitude waves produced by a rigid porous plate that is bottom-mounted in a channel of constant depth, is investigated. The solution of scattering and radiation problems, in both submerged and floating elastic porous plates, was further expanded by the work of [19]- [20], as wells as by, [21]and [22] who studied the hydroelastic behaviour of flexible submerged porous plates, in terms of wave energy absorption.

The interaction of waves with porous cylindrical bodies is another issue that has been particularly studied in the literature. The wave interaction of a porous free surface piercing cylindrical body with a coaxial inner impermeable cylinder was initially studied in [23], concluding in the fact that the existing of porous outer surface leads to reduced hydrodynamic forces in the inner cylinder. In order to evaluate wave kinematics around a protected cylindrical impermeable pile, an analytical methodology was developed and presented in [24]. Furthermore, the wave interaction with an array of bottom-mounted surface-piercing porous cylinders was investigated in [25] using an eigenfunction expansion method. This was further extended in [26] where the body interacting with the waves, is a free floating cylinder and its proven that its porosity directly affects the hydrodynamic loads. In [27] the problem of wave diffraction around a cylinder with porous upper wall and an inner column was studied, and concluded in that an increased porous coefficient lead to a reduced wave elevation around the body.The case of wave diffraction around a group of dual porous cylinders was numerically and experimentally studied in [28]. Similarly, numerical and experimental results regarding the hydrodynamics of a con-

centric twin perforated circular cylinder system were presented in [29]. Bao et al [30], applied the Haskind relations in order to evaluate the the eigenfunctions values of the fluid domain inside a semi-submerged porous circular cylinder and in order. This concluded to the derivation of a new damping term created by porosity. The case of an array of freely floating, porous, circular cylinders was investigated in [31]. In [32] the wave interaction with a single truncated cylinder was investigated and a theoretical method, that was also validated experimentally was developed. Theoretical and experimental results regarding an array of porous circular cylinders with impermeable bottom, supplemented by horizontal, porous plates inside the bodies were presented in [33].In addition, an array of partially porous, surface-piercing cylindrical bodies were examined in [34] with the development of a 3D numerical model. An optimal ratio of porous to impermeable portion of surface was adopted in order to minimize the hydrodynamic impact. In [35] they study the impact of geometrical characteristics and porous coefficient on the hydrodynamic loads on a truncated cylinder, and the proper selection of said values that will lead in reduced hydrodynamic loads. Furthermore, in [36], [37], the effect of linear and quadratic resistance laws on porous bodies of arbitrary shape was examined. Cong et al [38] applied the image method to study the effect of a vertical breakwater on the hydrodynamics of a bottom-mounted, porous cylinder that pierces the free surface and is placed in front of the wall. It was concluded that the presence of the porous cylinder can reduce the amplified wave effects that derive from the presence of the wall. In [39] the hydrodynamics of a moored porous cylindrical body are studied.

Another widely investigated subject in the literature of porous cylinders is the water wave interaction with fish-farm cages. In the recent decade some notable studies are [40]- [41], where a porous flexible circular cylinder is simulating the fish net. In order to further investigate wave interaction with fish cages, several computational models have been developed. For example, in [42] in the framework of potential theory and without taking under consideration the existence of currents, a slender-body theory is presented to simulate the wave effects on a floating fish cage. This study was further extended in [43] with the development of a numerical model capable of calculating viscous waves and current loads on fish nets. Continually, this was further developed in [44], [45] to taking into account the induced wave and current mooring loads on the fish cage nets. The mooring characteristics and behaviour of a elastic fish cage with a cubic shape was validated with experimental results and presented in [46]. In [47] the hydrodynamic response of a porous flexible circular-cylinder fish cage in regular waves was analytically studied where in [48] a semi analytical a model was developed describing the wave field around a submerged cylindrical fish net cage. Furthermore, in [] a numerical model to describe wave–current interactions with a moored flexible cylindrical cage was developed. It was further validated with numerical finite element model results. In [49] a semi-analytical solution to describe the interactions between waves and a flexible cylindrical net cage, the deformation of which is governed by the membrane vibration equation of cylindrical shells, is presented.

1.3 Thesis Objective

In the present study, a free floating, free surface piercing, porous cylindrical body is examined. The porous outer surface is assumed to be inflexible while the bottom of the body to be impermeable. The linearised problems of diffraction and radiation around the porous body are solved in the frequency domain according to the theoretical approach described thoroughly in the following chapters. The hydrodynamic problems of surge, heave and roll are resolved with

the implementation of matched axisymmetric eigenfunction expansions method. This method allows the subdivision of the flow field around and inside the body into coaxial, ring shaped fluid regions categorized by the numerals I, II, III (see 2.1), in each of which different series representations of the velocity potential are made. These series expansions are selected in such a way, that the kinematic boundary condition at the horizontal walls of the body, the kinematic condition on the sea bed, the radiation one at infinity and the linearised condition at the free surface,are a priori satisfied. The various solutions, that derived with the use of Galerkin method, are matched by the requirements for continuity of the hydrodynamic pressure and radial velocity along the vertical boundaries of adjacent fluid regions, as well as by fulfilling appropriate boundary conditions of the porous vertical walls of the body, that derived from the application of Darcy's linear law. The accuracy of the present study is validated by comparisons of data available in the existing literature. Lastly, the effect of porosity and radius on the body's exciting forces and moments, hydrodynamic coefficients of added mass and damping, and motions is investigated.

1.4 Thesis Structure

Chapter 1 briefly reviews the use and types of porous structures in offshore engineering, summarizes and reviews relevant to the present thesis literature, and presents the aim and structure of the thesis.

Chapter 2 presents the formulation of the problem, describes the boundary value problem, presents the analytical solutions for the hydrodynamic coefficients of added mass and damping and the solutions for the excitation forces and moments and describes the equation of motion of the body.

Chapter 3 presents results regarding the effect of porous coefficient G, body's radius and draught, on the permeable body's exciting forces and moment and hydrodynamic coefficients of added mass and damping, as well as on the body's motions. Furthermore, the numerical method used in this study is validated by comparisons of data, available in the existing literature.

Chapter 4 presents the conclusions drawn from the present study and suggests areas for future research.

Lastly, bibliographical references are listed.

2 Problem Formulation

2.1 Boundary Values Problem

In the present study the examined body is assumed to be, a free floating cylinder that pierces the free surface, has an impermeable thin bottom and a permeable outer surface. It is subjected to the action of regular waves of circular frequency ω and linear amplitude $(H/2)$ which propagate at a zero angle in a constant water depth of d. The radius of the body is denoted by α, the distance of the bottom of the body to the seabed is denoted by h, while the distance of the bottom porous surface (the top of the impermeable bottom) is denoted by h_1. The problem is described by a cylindrical coordinate system (r, θ, z) originating at the seabed and coinciding with the axis of symmetry of the body (see Figure 1). Furthermore, the fluid is assumed to be inviscid and incompressible while the flow irrotational.

It is assumed that the water domain is divided into three regions as follows, see Figure [2.1]:

- **flow region** I

  $r \geq a; \ 0 \leq z \leq d;$

- **flow region** II

  $0 \leq r \leq a; \ h_1 \leq z \leq d;$

- **flow region** III

  $0 \leq r \leq a; \ 0 \leq z \leq h;$
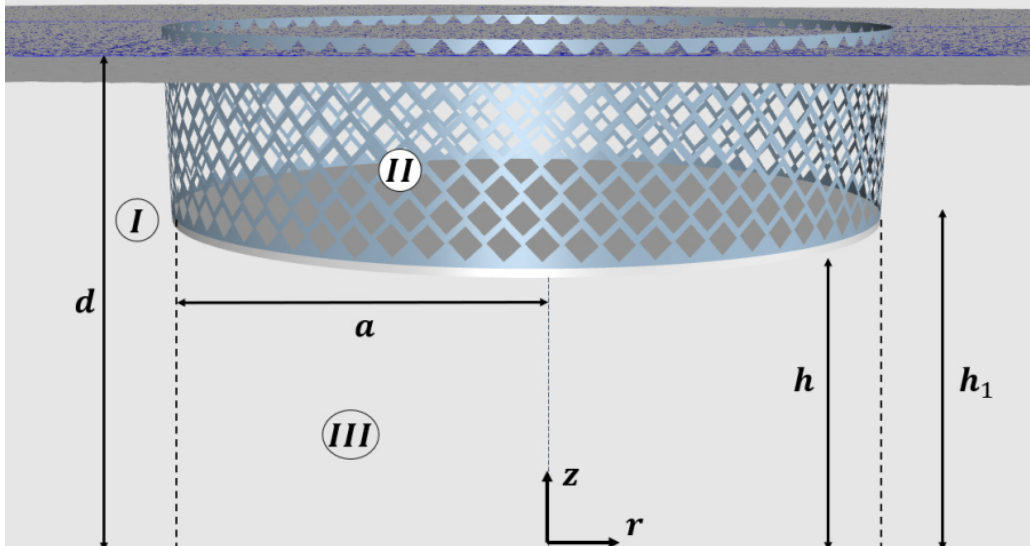
Figure 2.1: A 3D representation of the examined permeable vertical cylindrical body [39]

The assumption of irrotational flow allows the flow in each fluid region to be described in terms

of velocity potential as follows:

$$\Phi^k(r, \theta, z; t) = Re[\phi^k(r, \theta, z)e^{-i\omega t}], \ k = I, II, III \tag{2.1}$$

The linearisation of the problem leads to the decomposition of the potential function into three terms: the velocity potential due to undisturbed incident harmonic wave ϕ_0, the velocity potential related to the scattered disturbance of the incident waves from the body ϕ_s, the velocity potential of waves radiated due to the motion of the body ϕ_7. Further, we denote the velocity potential due to the diffracted waves ϕ_D. In the cases of ϕ_s and ϕ_D the body is considered to be stationary at its mean static equilibrium, whereas in the case of radiation potential ϕ_7 the body is considered to be performing forced oscillations at its motions of freedom in still liquid. The following equations describe the aforementioned velocity potentials and the relations between them.

The velocity potential of every fluid region can be described as:

$$\phi^k(r, \theta, z) = \phi_0(r, \theta, z) + \phi_7^k(r, \theta, z) + \sum_{j=1,3,5} \dot{\xi}_{j0} \ \phi_j^k(r, \theta, z), \ k = I, II, III \tag{2.2}$$

where $\dot{\xi}_{j0}$ is the complex velocity amplitude of body motion in the j-th direction.

While the diffraction problem is described by:

$$\phi_D^k(r, \theta, z) = \phi_0(r, \theta, z) + \phi_7^k(r, \theta, z), \ k = I, II, III \tag{2.3}$$

The velocity potential of the undisturbed incident wave can be expressed using Jacobis's expansion as:

$$\phi_0(r, \theta, z) = -i\omega \frac{H}{2} \frac{cosh(kz)}{ksinh(kd)} \sum_{m=0}^{\infty} \epsilon_m i^m J_m(kr) cos(m\theta) \tag{2.4}$$

where where J_m denotes the m-th order Bessel function of first kind and m the Neumann's symbol:

$$\epsilon_m = \begin{cases} 1, & m = 0 \\ 2, & m \geq 0 \end{cases} \tag{2.5}$$

The circular frequency ω and wave number k are related by the dispersion equation:

$$\omega^2 = gktanh(kd) \tag{2.6}$$

In accordance to Equation (2.4) the diffraction potential of the flow field around the body can be expressed as:

$$\phi_D^k(r, \theta, z) = -i\omega \frac{H}{2} \sum_{m=0}^{\infty} \epsilon_m i^m \Psi_{Dm}^k(r, z) cos(m\theta) \tag{2.7}$$

Similar to Equation (2.7) the radiation potentials can be described as:

$$\phi_1^k(r, \theta, z) = \Psi_{11}^k(r, z)cos(\theta) \tag{2.8}$$

$$\phi_3^k(r, \theta, z) = \Psi_{30}^k(r, z) \tag{2.9}$$

$$\phi_5^k(r, \theta, z) = \Psi_{51}^k(r, z)cos(\theta) \tag{2.10}$$

8

In the Equations (2.8) the first subscript $l = D, 1, 3, 5$ denotes the respective boundary value problem while the second one denotes the values of m that should be taken into account in the solution process. Therefore, the functions Ψ_{lm}^k, $k = I, II, II$ remain the main unknown of the problem.

The complex velocity potentials ϕ_j, $j = 0, 1, 3, 5, 7$ have to satisfy:

The Laplace equation in the entire corresponding fluid domain:

$$\Delta\phi_j^k = \frac{\partial^2\phi_j^k}{\partial r^2} + \frac{1}{r}\frac{\partial\phi_j^k}{\partial r} + \frac{1}{r^2}\frac{\partial^2\phi_j^k}{\partial\theta^2} + \frac{\partial^2\phi_j^k}{\partial z^2}, \; k = I, II, III \tag{2.11}$$

The free surface boundary condition:

$$-\omega^2\phi_j^k + g\frac{\partial\phi_j^k}{\partial z} = 0, \; z = d; \; k = I, II \tag{2.12}$$

And the impermeable boundary condition at the seabed:

$$\frac{\partial\phi_j^k}{\partial z} = 0, \; z = 0; \; k = I, III \tag{2.13}$$

In addition, the radiation and scattering potentials $\phi_j, j = 1, 3, 5, 7$ have to fulfil the Somerfield radiation condition at the far-field [50]:

$$\lim_{r\to\infty} \sqrt{kr}\left(\frac{\partial\phi_j^k}{\partial r} - ik\phi_j^k\right) = 0 \tag{2.14}$$

Furthermore, the kinematic condition at the impermeable wetted surface S of the body, in its average position, has to be satisfied:

$$\frac{\partial\phi_7^k}{\partial n} = -\frac{\partial\phi_0}{\partial n} = 0, \; \text{on } S \tag{2.15}$$

and,

$$\frac{\partial\phi_j^k}{\partial n} = n_j, \; \text{on } S; \; j = 1, 3, 5 \tag{2.16}$$

In Equations (2.15) and (2.16) $\frac{\partial}{\partial n}$ denotes the derivative in the direction of the outward unit normal vector, n, to the mean wetted surface of the body and n_j is the generalised normal vector defined as:

$$(n_1, n_2, n_3) = n \tag{2.17}$$

and

$$(n_4, n_5, n_6) = r \times n \tag{2.18}$$

where r is the position vector with respect to the origin of the coordinate system.

The flow through the porous openings of the body's sidewall is characterized by relatively small Reynold's numbers, so it can be assumed to obey the linear Darcy's law [51]. The normal flow velocity is assumed to be continuous and linearly proportional to the pressure difference through the porous boundary [25]. Hence, the boundary condition on the porous surface of the body forms:

$$\frac{\partial\phi_j^{II}}{\partial r} = n_j + ikG(\phi_{II} - \phi_I) \; on \; r = a, \; h_1 \leq z \leq d, \; j = 1, 3, 5, D \tag{2.19}$$

where G denotes the complex dimensionless porous effect parameter. This coefficient can be composed as $G = G_{re} + iG_{im}$, where G_{re} is its real part representing the linearised drag effect

on the porous sidewall and G_{im} its imaginary part, representing the inertial effect. Therefore, for a real G, the resistance effects dominate over inertia effects, while G acquires complex values when inertia effects dominate over resistance ones. The parameter G also expresses a measure for the porosity effect, when its value tends to zero $G = 0$ the sidewall is completely impermeable, while when it tends to values much higher than unity, $G >> 1$, the sidewall is completely permeable, i.e. there is no sidewall. In [], it was proven experimentally that the porous coefficient G is related to the opening rate τ of the material, the ratio between the area of the opening holes and the total area, as well as the waveslope $\epsilon = \frac{kH}{2}$, through the following Equation:

$$G = \frac{(\frac{17.8}{\epsilon} + 432.2)\tau^2}{2\pi(1 + 1.06\tau)} \tag{2.20}$$

As the flow is considered to be continuous on either side of the boundary, both the velocity potential and its derivative must be continuous at at the vertical boundaries of adjacent fluid regions.

- at $r = a$ for $0 \leq z \leq h$

$$\phi_j^I = \phi_j^{III} \tag{2.21}$$

$$\frac{\partial \phi_j^I}{\partial r} = \frac{\partial \phi_j^{III}}{\partial r} \tag{2.22}$$

- at $r = a$ for $h_1 \leq z \leq d$

$$\frac{\partial \phi_j^I}{\partial r} = \frac{\partial \phi_j^{II}}{\partial r} \tag{2.23}$$

2.2 Analytical Solutions

- Infinite flow region I

$$\frac{1}{\delta_j}\Psi_{lm}^I(r,z) = f_{lm}^I(r,z) + \sum_{i=0}^{\infty} F_{lm,i}^I \frac{K_m(a_i^I r)}{K_m(a_i^I a)} Z_i(z) \tag{2.24}$$

where K_m is the m-th order modified Bessel function of the second kind and $\delta_l = d$, for $l = D, 1, 3$ and $\delta_5 = d^2$. Whereas, the term f_{lm}^I equals to:

$$f_{11}^I = f_{30}^I = f_{50}^I = 0 \tag{2.25}$$

and

$$f_{Dm}^I = (J_m(kr) - \frac{J_m(ka)}{H_m(ka)}H_m(kr))\frac{Z_0(z)}{d\acute{Z}_0(z)} \tag{2.26}$$

where the term H_m is the m-th order Hankel function of the first kind.
The terms $Z_i(z)$, in Equations (2.24) and (2.45), are the orthonormal functions in $[0, d]$ defined as follows:

$$Z_0(z) = N_{0,I}^{-\frac{1}{2}} cosh(k^I z) \tag{2.27}$$

$$Z_i(z) = N_{i,I}^{-\frac{1}{2}} cosh(a_i^I z) \tag{2.28}$$

where

$$N_{0,I} = \frac{1}{2}[1 + \frac{sinh(2k^I d)}{2k^I d}] \tag{2.29}$$

$$N_{i,I} = \frac{1}{2}[1 + \frac{sinh(2a_i^I d)}{2a_i^I d}] \tag{2.30}$$

The wave number $k^I \equiv k$ and is related to ω through the dispersion relation (Equation (2.6)).

The terms a_i^I are the positive real roots of the transcendental equation:

$$\frac{\omega^2}{g} + a_i^I tan(a_i^I d) = 0 \tag{2.31}$$

and the imaginary root $a_0^I = -ik$.

- Second flow region II

$$\frac{1}{\delta_j}\Psi_{lm}^{II}(r,z) = f_{lm}^{II}(r,z) + \sum_{i=0}^{\infty} F_{lm,i}^{II} \frac{I_m(a_i^{II}r)}{I_m(a_i^{II}a)} Z_i(z - h_1) \tag{2.32}$$

where the term I_m is the m-th order modified Bessel function of the first kind and the term f_{lm}^{II} is equal to:

$$f_{Dm}^{II} = f_{11}^{II} = 0 \tag{2.33}$$

$$f_{30}^{II} = \frac{z}{d} - 1 + \frac{g}{d\omega^2} \tag{2.34}$$

$$f_{51}^{II} = -\frac{r}{d^2}((z - d) + \frac{g}{\omega^2}) \tag{2.35}$$

Where the term $Z_i(z - h_1)$ is derived as follows:

$$Z_0(z - h_1) = N_{0,II}^{-\frac{1}{2}}cosh(k^{II}(z - h_1)) \tag{2.36}$$

$$Z_i(z - h_1) = N_{i,II}^{-\frac{1}{2}}cosh(a^{II}(z - h_1)) \tag{2.37}$$

where

$$N_{0,II} = \frac{1}{2}[1 + \frac{sinh(2k^{II}(d - h_1))}{2k^{II}(d - h_1)}] \tag{2.38}$$

$$N_{i,II} = \frac{1}{2}[1 + \frac{sin(2a^{II}(d - h_1))}{2a^{II}(d - h_1)}] \tag{2.39}$$

The terms a_i^{II} are the roots of the transcendental equation:

$$\frac{\omega^2}{g} + a_i^{II}tan(a_i^{II}(d - h_1)) = 0 \tag{2.40}$$

with the imaginary root $a_i^{II} = -ik^{II}$ to be considered as first.

- Third flow region III

$$\frac{1}{\delta_j}\Psi_{lm}^{III}(r,z) = f_{lm}^{III}(r,z) + \sum_{n=0}^{\infty} \epsilon_m F_{lm,n}^{III} \frac{I_m(\frac{n\pi}{h}r)}{I_m(\frac{n\pi}{h}a)} cos(\frac{n\pi}{h}z) \tag{2.41}$$

where the term f_{lm}^{III} equals to:

$$f_{Dm}^{III} = f_{II}^{III} = 0 \tag{2.42}$$

$$f_{30}^{III} = \frac{z^2 - 0.5r^2}{2hd} \tag{2.43}$$

$$f_{51}^{III} = \frac{-r(z^2 - 0.25r^2)}{2hd^2} \tag{2.44}$$

11

2.3 Hydrodynamic Forces

The various hydrodynamic forces acting on the permeable body are calculated by the pressure distribution given by the linearized Bernoulli's equation. Therefore they can be written as:

$$F_1 = -2\pi i \rho \omega^2 d\frac{H}{2}a[\int_h^d \frac{1}{d}\Psi_{D1}^I(a,z)dz - \int_{h1}^d \frac{1}{d}\Psi_{D1}^{II}(a,z)dz] \tag{2.45}$$

Given the Equations (2.24) and (2.32)), Equation (2.45) becomes:

$$\frac{F_1}{B} = -2ikdtanh(kd)[N_{0,I}^{-\frac{1}{2}}F_{D1,0}^I\frac{sinh(kd)-sinh(kh)}{ka} + \sum_{i=1}^{\infty}N_{i,I}^{-\frac{1}{2}}F_{D1,i}^I\frac{sin(a_i^I d)-sin(a_i^I h)}{a_i^I a}]$$
$$- N_{0,II}^{-\frac{1}{2}}F_{D1,0}^{II}\frac{sinh(k^{II}(d-h_1))}{k^{II}a} - \sum_{i=1}^{\infty}N_{i,II}^{-\frac{1}{2}}F_{D1,i}^{II}\frac{sin(a_i^{II}(d-h_1)))}{a_i^{II}a}] \tag{2.46}$$

where $B = \pi\rho g a^2(\frac{H}{2})$, ρ is the water density of seawater, g is the gravity acceleration. Accordingly, the vertical forces acting on the permeable body are equal to the sum of the forces acting on the upper surface ($0 \leq r \leq a$; $z = h_1$) and lower surface ($0 \leq r \leq a$; $z = h$). Therefore,

$$F_3 = 2\pi\rho\omega^2 d\frac{H}{2}[\int_0^a \frac{1}{d}\Psi_{D0}^{III}(r,h)rdr - \int_0^a \frac{1}{d}\Psi_{D0}^{II}(r,h_1)rdr] \tag{2.47}$$

When substituting Equations (2.32) and (2.41) in Equation (3.12b), we get

$$\frac{F_3}{B} = 2kdtanh(kd)[\frac{1}{2}F_{D0,0}^{III} + 2\sum_{i=1}^{\infty}(-1)^n F_{D0,i}^{III}\frac{1}{\frac{n\pi a}{h}}\frac{I_1(\frac{n\pi}{h}a)}{I_0(\frac{n\pi}{h}a)}]$$
$$- N_{0,II}^{-\frac{1}{2}}F_{D0,0}^{II}\frac{1}{k^{II}a}\frac{J_1(k^{II}a)}{J_0(k^{II}a)} - \sum_{i=1}^{\infty}N_{i,II}^{-\frac{1}{2}}F_{D0,i}^{II}\frac{1}{a_i^{II}}\frac{I_1(a_i^{II}a)}{I_0(a_i^{II}a)}] \tag{2.48}$$

The moment on the permeable body about a horizontal axis in arbitrary distance $z = e$ from the seabed can be analysed in terms of M_S and M_b obtained from the distribution of pressure on the wetted surfaces of the body, both permeable and impermeable, and it holds:

$$M_S = -2i\pi\rho\omega^2 d\frac{H}{2}a[\int_h^d \frac{1}{d}\Psi_{D1}^I(a,z)(z-e)dz - \int_{h_1}^d \frac{1}{d}\Psi_{D1}^{II}(a,z)(z-e)dz] \tag{2.49}$$

$$M_b = -2\pi\rho\omega^2 d\frac{H}{2}[\int_0^2 \frac{1}{d}\Psi_{D1}^{III}(r,h)r^2 dr - \int_0^a \frac{1}{d}\Psi_{D1}^{II}(r,h_1)r^2 dr] \tag{2.50}$$

Substituting Equations (2.24), (2.32), and (2.41) into Equations (2.49) and (2.50), it is derived that

$$\frac{M_S}{Ba} = -2ikdtanh(kd)[-N_{0,I}^{-\frac{1}{2}}F_{D1,0}^I L_0^I + \sum_{i=1}^{\infty}N_{i,I}^{-\frac{1}{2}}F_{D1,i}^I L_i^I - N_{0,II}^{-\frac{1}{2}}F_{D1,0}^{II} L_0^{II} - \sum_{i=1}^{\infty}N_{i,II}^{-\frac{1}{2}}F_{D1,i}^{II} L_i^{II}] \tag{2.51}$$

$$\frac{M_b}{Ba} = -2kdtanh(kd)[\frac{1}{4}F_{D1,0}^{III} + 2\sum_{i=1}^{\infty}(-1)^n F_{D1,i}^{III}\frac{1}{\frac{n\pi a}{h}}\frac{I_2(\frac{n\pi}{h}a)}{I_1(\frac{n\pi}{h}a)}$$

$$-N_{0,II}^{-\frac{1}{2}}F_{D1,0}^{II}\frac{1}{k^{II}a}\frac{J_2(k^{II}a)}{J_1(k^{II}a)} - \sum_{i=1}^{\infty}N_{i,II}^{-\frac{1}{2}}F_{D1,i}^{II}\frac{1}{a_i^{II}}\frac{I_2(a_i^{II}a)}{I_1(a_i^{II}a)}] \tag{2.52}$$

where the terms $L_0^I, L_0^{II}, L_i^I, L_i^{II}$ are defined as follows,

$$L_0^I = \frac{k(d-e)sinh(kd) - k(h-e)sinh(kh) - cosh(kd) + cosh(kh)}{(ka)^2} \tag{2.53}$$

$$L_i^I = \frac{a_i^I(d-e)sin(a_i^I d) - a_i^I(h-e)sin(a_i^I h) + cos(a_i^I d) - cos(a_i^I h)}{(a_i^I a)^2} \tag{2.54}$$

$$L_0^{II} = \frac{-1 - k^{II}(d-e)sinh(k^{II}(d-h_1)) + cosh(k^{II}(d-h_1))}{(k^{II}a)^2} \tag{2.55}$$

$$L_i^{II} = \frac{-1 + a_i^{II}(d-e)sin(a_i^{II}(d-h_1)) + cos(a_i^{II}(d-h_1))}{(a_i^{II}a)^2} \tag{2.56}$$

Similarly due to the permeable body's sinusoidal motion in the the i-th direction with frequency *omega* and unit amplitude in the j-th direction, the corresponding reaction forces and pitching moment F_{ij} equal to:

$$F_{ij} = -\rho\omega^2 \iint\limits_{S} \Psi_{j0}^y(r,z)cos(m\theta)n_i dS, \ y = I, II, III; \ i,j = 1,3,5 \tag{2.57}$$

where S stands for the wetted surface and n_i as defined in Equation (2.16). Furthermore, Equation (2.57) can also be written as:

$$F_{ij} = \omega^2 a_{ij} + i\omega b_{ij} \tag{2.58}$$

where a_{ij} and b_{ij} denote the hydrodynamic mass and damping coefficients in the i-th direction due to the unit sinusoidal motion of the body in the j-th direction. It is worth noted that both a_{ij} and b_{ij} are real and ω-dependent.

Substituting Equations (2.24), (2.32) and (2.41) into equation (2.58) gives the following relationships for the non-dimensional hydrodynamic coefficients:

$$\frac{a_{11}}{\rho a^3} + i\frac{b_{11}}{\rho\omega a^3} = -\pi\frac{d}{a}[N_{0,I}^{-\frac{1}{2}}F_{11,0}^I\frac{sinh(kd) - sinh(kh)}{ka} + \sum_{i=1}^{\infty}N_{i,I}^{-\frac{1}{2}}F_{11,i}^I\frac{sin(a_i^I d) - sin(a_i^I h)}{a_i^I a}$$

$$-N_{0,II}^{-\frac{1}{2}}F_{11,0}^{II}\frac{sinh(k^{II}(d-h_1)}{k^{II}a} - \sum_{i=1}^{\infty}N_{i,II}^{-\frac{1}{2}}F_{11,i}^{II}\frac{sin(a_i^{II}(d-h_1))}{a_i^{II}a}] \tag{2.59}$$

$$\frac{a_{33}}{\rho a^3} + i\frac{b_{33}}{\rho\omega a^3} = 2\pi\frac{d}{a}[(\frac{h}{4d} - \frac{a^2}{16hd} + \frac{1}{2}F_{33,0}^{III} + 2\sum_{n=1}^{\infty}(-1)^n F_{33,i}^{III}\frac{1}{\frac{n\pi a}{h}}\frac{I_1(\frac{n\pi a}{h})}{I_0(\frac{n\pi a}{h})}$$

$$-\frac{1}{2}(\frac{h_1}{d} - 1 + \frac{g}{\omega^2 d}) - N_{0,II}^{-\frac{1}{2}}F_{30,0}^{II}\frac{1}{k^{II}a}\frac{J_1(k^{II}a)}{J_0(k^{II}a)} - \sum_{i=1}^{\infty}N_{i,II}^{-\frac{1}{2}}F_{30,i}^{II}\frac{1}{a_i^{II}a}\frac{I_1(a_i^{II}a)}{I_0(a_i^{II}a)} \tag{2.60}$$

$$\frac{a_{55}}{\rho a^5} + i\frac{b_{55}}{\rho \omega a^5} = -\pi\frac{d^2}{a^2}(M_S + M_B) \tag{2.61}$$

The terms M_S and M_B are defined as follows:

$$M_S = N_{0,I}^{-\frac{1}{2}} F_{51,0}^I L_0^I + \sum_{i=1}^{\infty} N_{i,I}^{-\frac{1}{2}} F_{51,i}^I L_i^I - N_{0,II}^{-\frac{1}{2}} F_{51,0}^{II} L_0^{II} + \sum_{i=1}^{\infty} N_{i,II}^{-\frac{1}{2}} F_{51,i}^{II} L_i^{II} \tag{2.62}$$

$$
\begin{aligned}
M_B = {} & \frac{1}{8}\frac{ah}{d^2} - \frac{1}{48}\frac{a^3}{d^2 h} + \frac{1}{4}F_{51,0}^{III} + 2\sum_{n=1}^{\infty}(-1)^n F_{51,i}^{III}\frac{1}{\frac{n\pi a}{h}}\frac{I_2(\frac{n\pi a}{h})}{I_1(\frac{n\pi a}{h})} - \frac{ag}{4d^2\omega} + \frac{a(d-h_1)}{4d^2} \\
& - N_{0,II}^{-\frac{1}{2}} F_{51,0}^{II}\frac{1}{k^{II}a}\frac{J_2(k^{II}a)}{J_1(k^{II}a)} - \sum_{i=1}^{\infty} N_{i,II}^{-\frac{1}{2}} F_{51,i}^{II}\frac{1}{a_i^{II}a}\frac{I_2(a_i^{II}a)}{I_1(a_i^{II}a)}
\end{aligned}
\tag{2.63}
$$

The terms $L_0^I, L_i^I, L_0^{II}, L_i^{II}$ are defined in Equations (2.53)-(2.56.

2.4   Equations of Motions

In the present study, the assumption of small motions and rotations in the free floating body's six degrees of freedom is made. This allows the the motions and rotation of the body to be calculated as follows:

$$\sum_{j=1}^{6}[-\omega^2(m_{ij} + a_{ij}) - i\omega b_{ij} + c_{ij}]x_{j0} = F_i \tag{2.64}$$

The terms m_{ij} in Equation 2.64 denote the generalized masses of the floating body, a_{ij} and b_{ij} the hydrodynamic added mass and damping coefficients respectively,c_{ij} the hydrostatic stiffness coefficients and F_i the exciting forces and moments.

The free floating permeable cylinder body is assumed to have symmetrical distribution of mass and to perform two translations moves, more precisely surge and heave, and one rotational move, pitch. Following these assumptions, the motions can be expressed in terms of response amplitude operator (RAOs) as follows:

$$\text{RAO}_i = \frac{x_{j0}}{H/2}, \ \text{i=1,3} \tag{2.65}$$

and

$$\text{RAO}_5 = \frac{x_{j0}}{kH/2}, \ \text{i=5,} \tag{2.66}$$

where k denotes the wave number.

2.5   Response Spectrum

The response spectrum results from the transformation of wave energy into response energy of a floating body in the frequency domain. The principle of this transformation is shown in Figure [2.3]. for the heave motions being considered here.
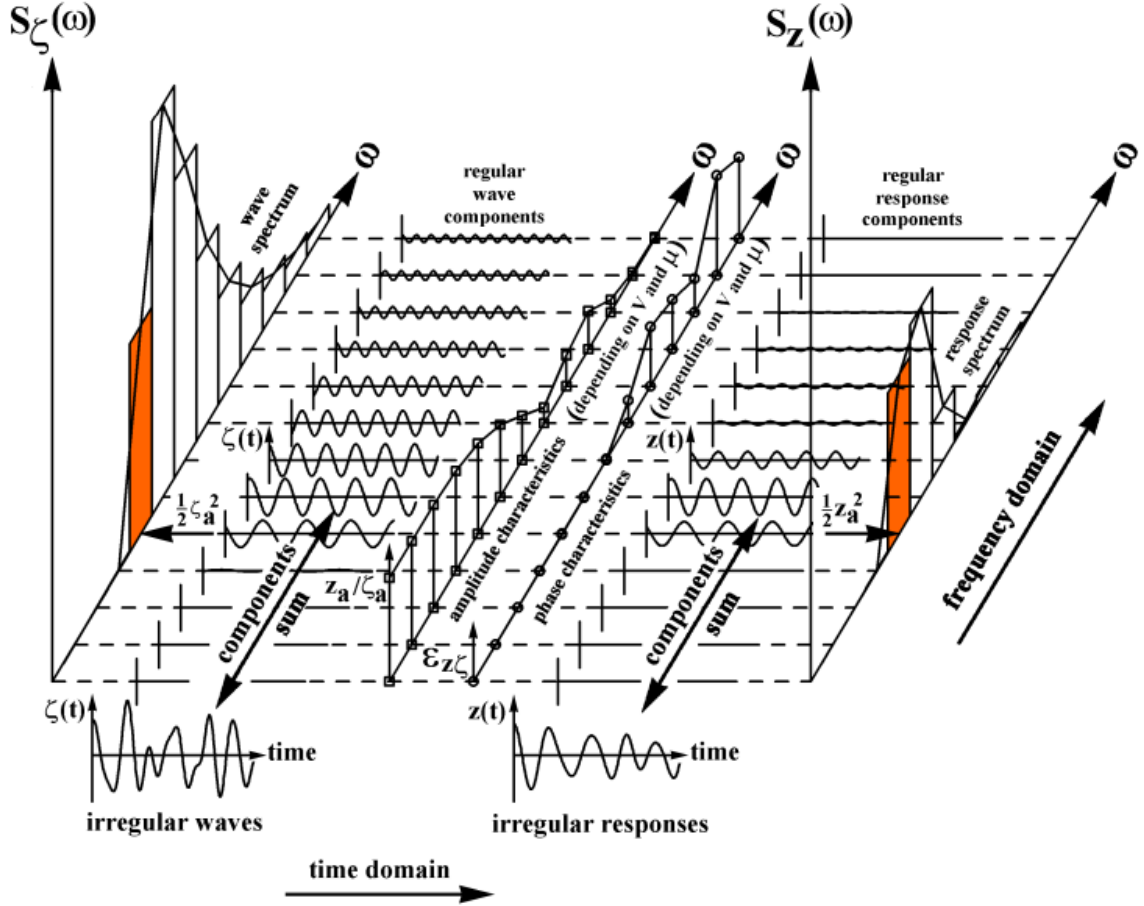
Figure 2.2: Principle of Transfer of Waves into Responses [52]

In Figure [2.3] the wave spectrum is depicted by $S_\zeta(\omega)$ and the term $\zeta(t)$ denotes the irregular wave history, which in terms of the linear wave theory, is the sum of regular waves components, each one with its own frequency, amplitude and energy. Figure [2.3] also shows the the response spectra for heave motion, denoted as $S_z(\omega)$. The regular heave components are obtained by multiplying each of the wave components by the motion RAO and then superpositioned to obtain the irregular heave history, $z(t)$.

2.5.1 JONSWAP Spectrum

It is known that, the wave spectrum describes the distribution of energy between wave components of different frequencies of a sea state. Wave spectra can be obtained directly from measured data. However, various mathematical formulas of wave spectra are available based on analysis of measured data, most notably, for fetch-limited regions, the Joint North Sea Wave Project (JONSWAP). The spectral density of the JONSWAP spectrum is described by [53]:

$$S_\zeta(\omega) = A_\gamma S_{PM}(\omega)\gamma^{exp[-\frac{1}{2}(\frac{\omega-\omega_p}{\sigma\omega_p})^2]} \tag{2.67}$$

where,

- $A_\gamma = 1 - 0.287 ln(\gamma)$
- $\gamma = 3.3$ peakedness factor

15

- $S_{PM}(\omega) = \frac{5}{16}(H_s^2 \omega_p^4)\omega^{-5} exp(-\frac{5}{4}(\frac{\omega}{\omega_p})^{-4})$

- $\sigma = \begin{cases} 0.07 \ (\omega \leq \omega_p) \\ 0.09 \ (\omega \geq \omega_p) \end{cases}$

where ω and ω_p are the the incident wave frequency and modal frequency, respectively. A_γ is the normalising factor with γ referring to the non-dimensional peak-enhancement factor. $S_{PM}(\omega)$ is the Pierson-Moskowitz spectrum, H_s is the significant wave height, and σ denotes the spectral width parameter as shown in Figure [2.3].
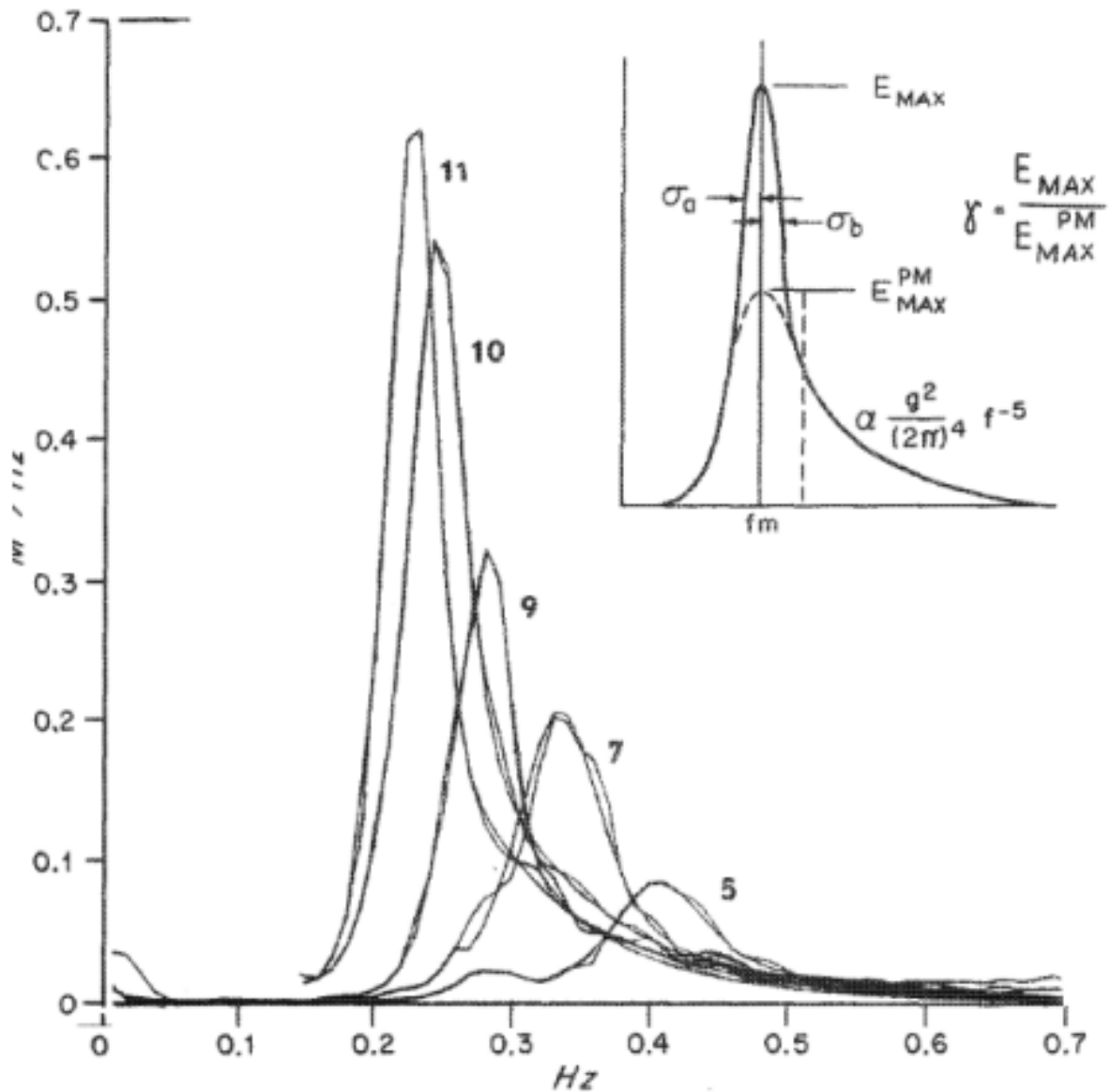
Figure 2.3: Measured wave spectra under ideal conditions and parametrical approximations. Principal sketch of the peak shape parameters γ, σ_a and σ_b. [53]

2.5.2 Climate Data

In this study, various values of climate data, significant wave height H_s and spectral period T_p were used to calculate the response spectrum of the examined body correspond. The upper limit of those values was determined by the maximum significant wave height H_s and the corresponding spectral wave period T_p as calculated in [54], for a given location in Greek seas.

H_s (m)	5.48
T_p (s)	10.28

Table 1: Climate Data

3 Results

3.1 Validation

In order to validate the numerical method used in the present study, its results are compared to corresponding ones available in the literature. The following results are produced by code developed in FORTRAN. The examined body is a porous free floating cylinder with a radius of a, draught ($d - h_1/a = 2$) that has an impermeable bottom, of negligible thickness and is subjected to waves propagating at zero angle in a constant water depth of $d = 100a/3$.

The porous coefficient G is assumed to be a real number and equal to G=1.432. As can be seen, in Figures 1 and 2 the hydrodynamic coefficients and exciting forces respectively are in total accordance to the results reported in [32]. In order for them to be comparable, the exciting forces and moment have been normalized by $\rho g a^2/(H/2)$ and $\rho g a^3/(H/2)$ while the hydrodynamic added mass and damping by ρa^3 and $\rho \omega a^3$ respectively.
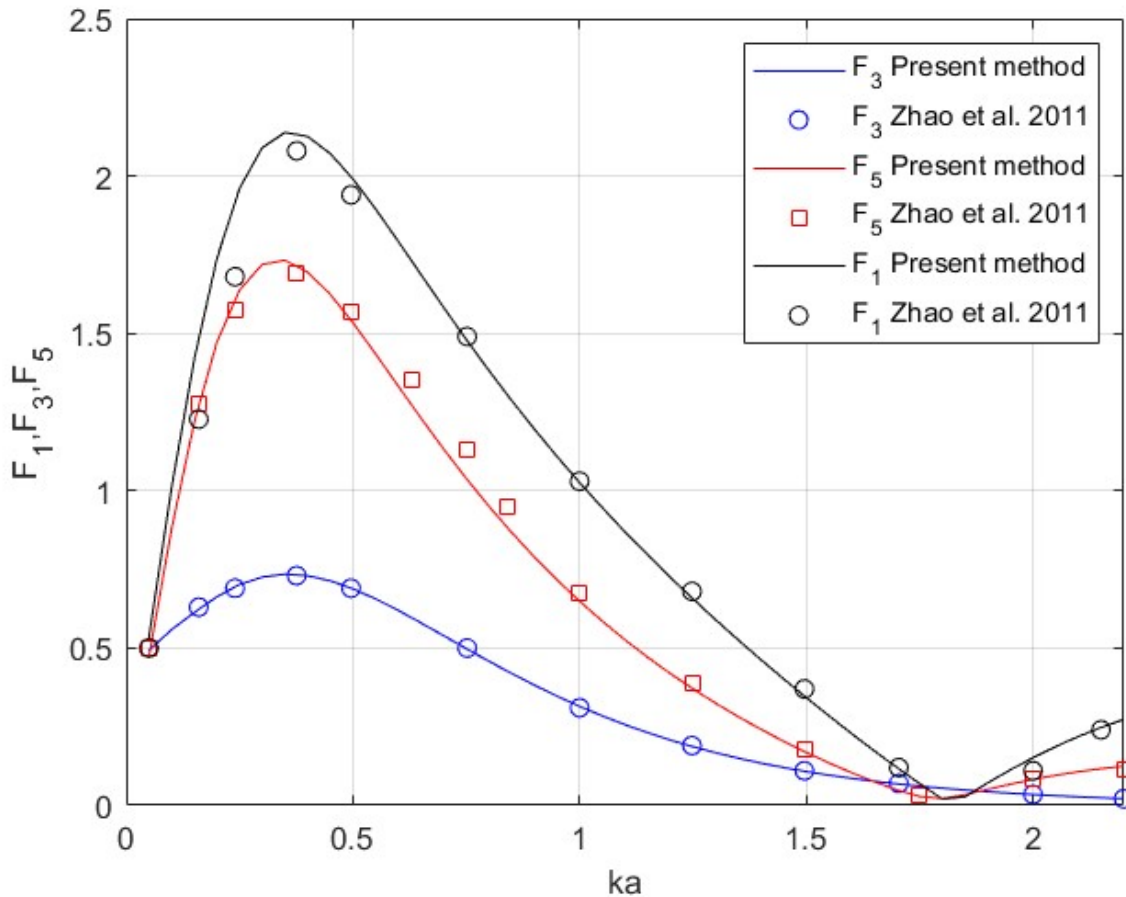
Figure 3.1: Comparison of the present method results against those from Zhao et al. the exciting forces and moments on a porous cylinder

(a)   (b)
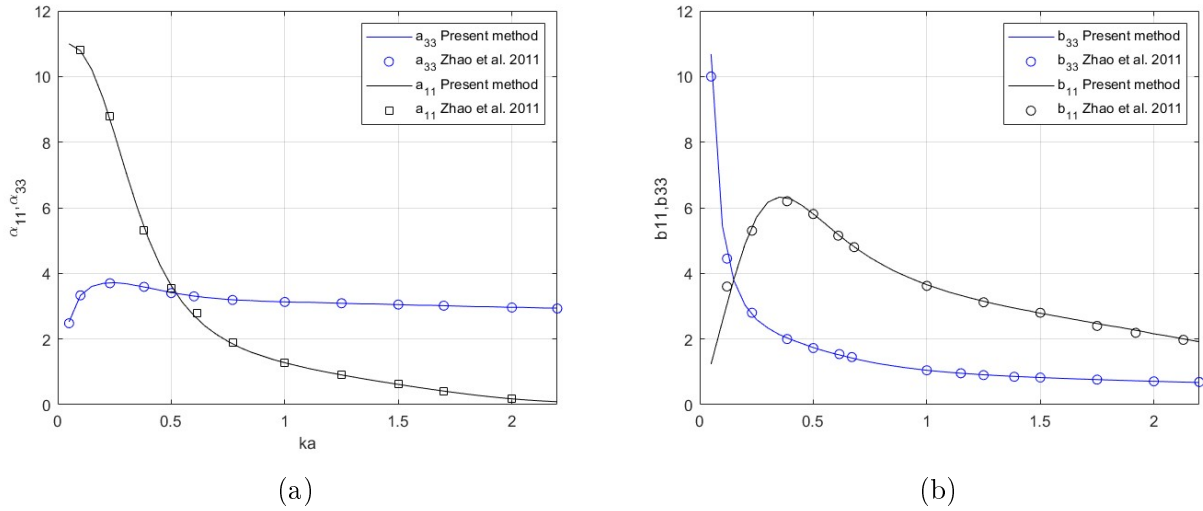
Figure 3.2: Comparison of the present method results against those due to Zhao et al. [32], concerning the hydrodynamic added mass in surge and heave (3.2a), hydrodynamic damping coefficients in surge and heave (3.2b)

.

3.2 Test Cases

3.2.1 Effect of the Porous G coefficient

In this section the effect of the porous coefficient in the exciting forces and hydrodynamic coefficients is explored. The examined body is, as aforementioned, a porous free floating cylinder with a radius of $a = 0.15$, draught $(d-h_1)/a = 2$ that has an impermeable bottom, of negligible thickness and is subjected to waves propagating at zero angle in a constant water depth of $d = 100\alpha/3$. The body's mass is assumed to be constant regardless of the porosity and equal to $M = 3.62 * 10^{-4}$ t, the center of gravity is located at the body's vertical axis at 4.697 m below the free surface and the mass moment of inertia relative to the free surface equals to $I_z = 4.075 * 10^{-6}$ tm^2

In Table 1 (2) the values of opening ratios τ and the corresponding values of G, as derived from the Equation (2.20), are depicted . The wave slope is considered to be $\epsilon = 0.05$ [36]. Furthermore, the cases of $G = 0$ and $G >> 1$, the body being fully impermeable and fully permeable respectively, are considered.

τ	0.037	0.08	0.12	0.14	0.22	0.41	0.60
G	0.101	0.468	1.015	1.432	3.118	9.309	17.482

Table 2: Opening ratios τ and the corresponding porous coefficient G for wave slope $\epsilon = 0.05$

The effect the porous coefficient G has on the surge, heave and pitch exciting forces and moment is depicted in Figure [3.3], while the effect on the corresponding hydrodynamic coefficients of added mass and damping is depicted in Figures [3.4]-[3.5].
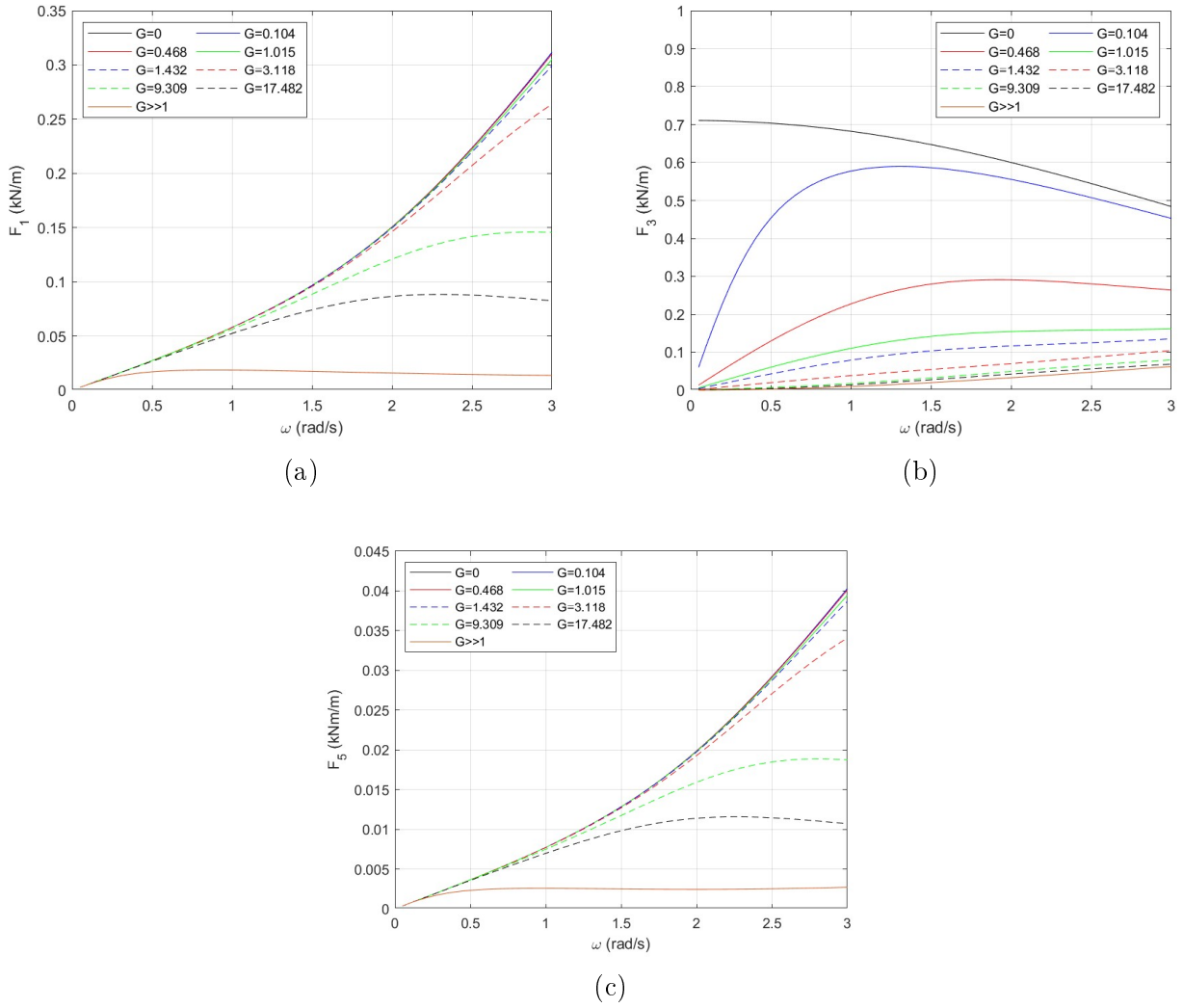
Figure 3.3: Exciting forces F_1, F_3 and moment F_5 on the permeable cylindrical body against wave frequency ω for various values of porous effect parameter

In Figure [3.3b], it can be clearly seen that the heave exciting forces behave differently for $G = 0$ and $G > 0$. For the case of impermeable cylinder, $G = 0$, the heave exciting force has a value of about 0.7 kN/m for $\omega \simeq 0$ whereas in the same frequencies, for cases of $G > 0$, F_3 tends to zero as G increases. This pattern, the decline of F_3 as G increases, is also observed at higher frequencies. It is also worth noted, that as G increases the local maxima of F_3 are observed in higher frequencies. As far as the surge excitation force F_1, Figure [3.3a], and the overturning moment F_5, Figure [3.3c], are concerned, the effect of G is not significant in the lower frequency range $\omega < 1$ rad/s. However, as the frequencies become higher, it becomes clearer that again, as the value of G increases, the excitation force and the overturning moment decrease. This holds true for all cases of G except of the fully submerged plate, $G >> 1$ where both F_1 and F_5 have a constant value for frequencies greater than $\omega = 0.2$ rad/s.
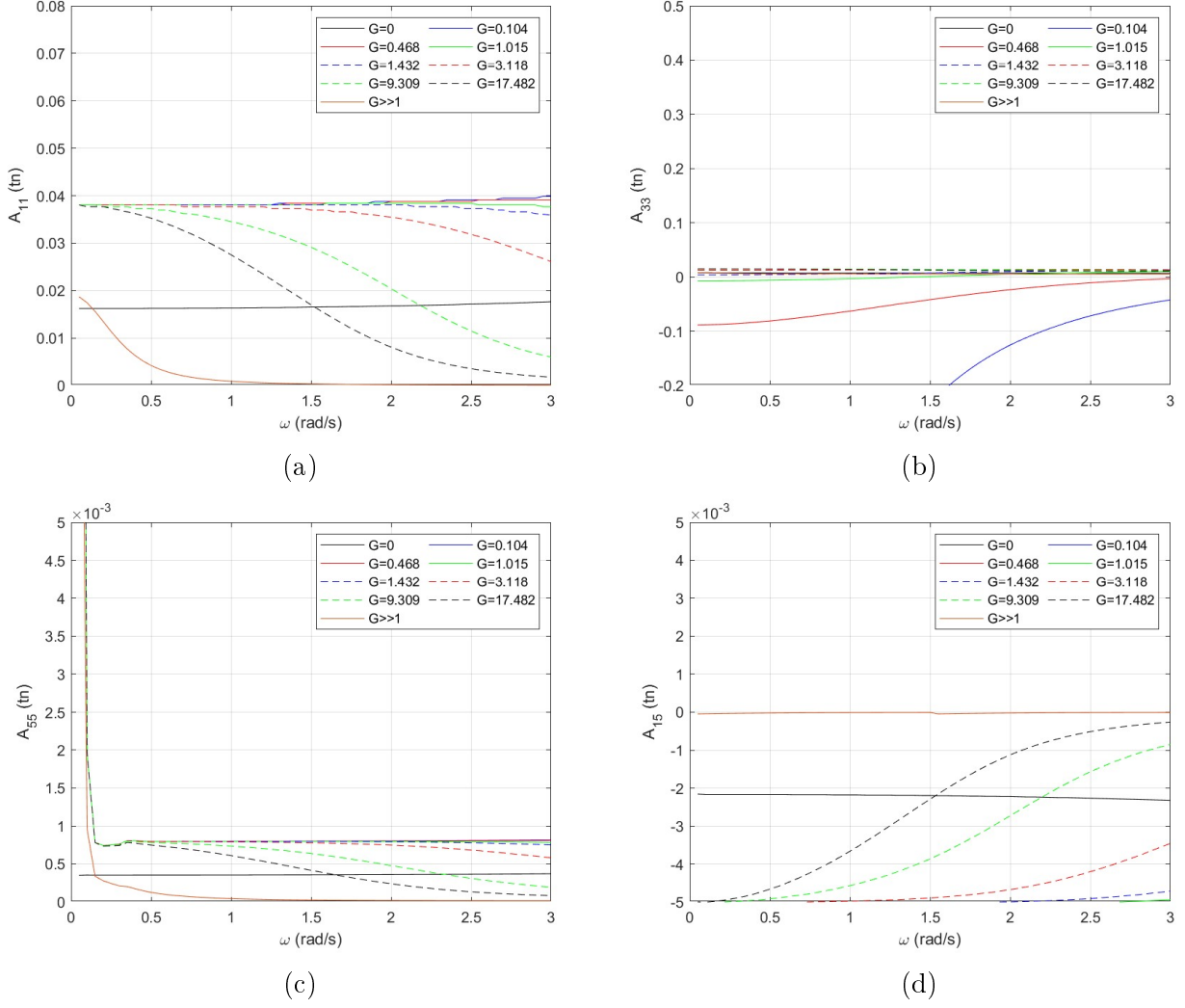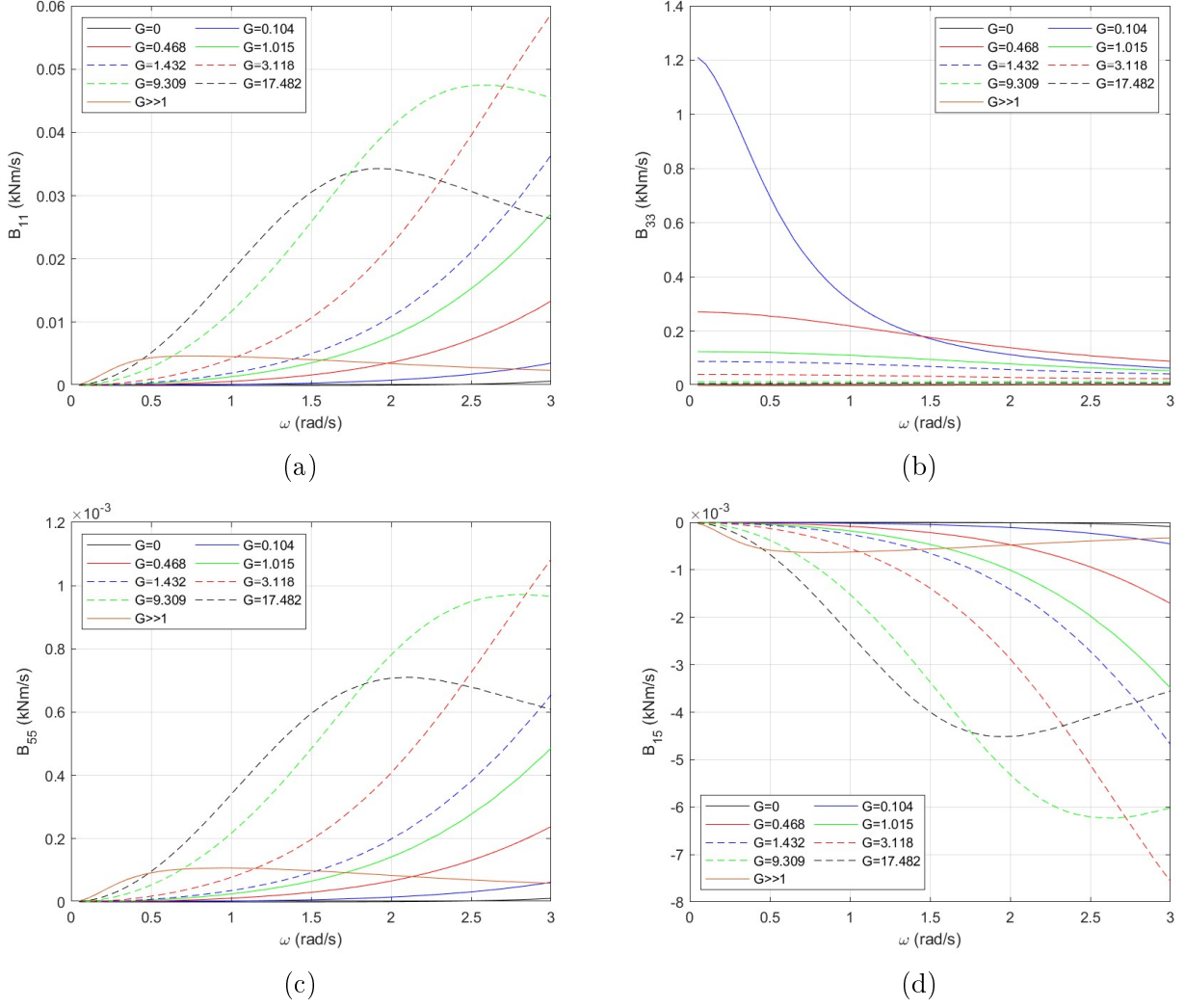
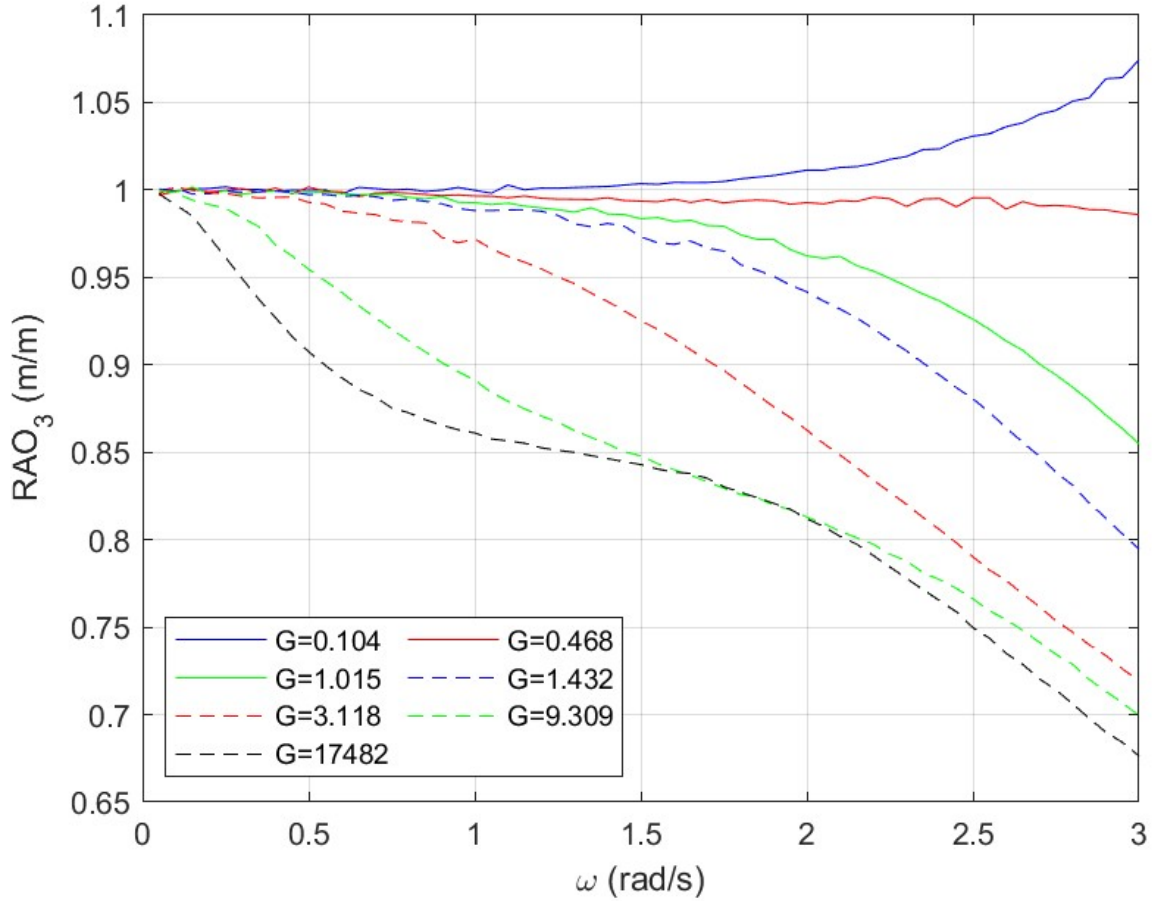Figure 3.4: Hydrodynamic added mass A_{11} A_{33}, A_{55} A_{15} of the permeable cylindrical body against wave frequency ω for various values of porous effect parameter.

Regarding the added mass in the wave direction, as depicted in figure [3.4a], it is noted that A_{11} decreases as G increases and gradually tends to zero in the higher frequency range. This trend is more evident in the case of higher values of G and especially in the case of the fully submerged plate, $G >> 1$, which exhibits a steeper decline towards zero. As far as, heave added mass, A_{33}, is concerned, it can be seen in Figure [3.4b] that for low frequencies, the added mass behaves proportionally to G, meaning it increases as G does, tending to the values of the submerged plate case $G >> 1$. It is worth noted that the pitch added mass A_{55}, as can be observed in Figure [3.4c],is characterized by the existence of local maxima at the lower frequency range $\omega < 0.2 \ rad/s$ for all cases of G, expect the one of impermeable cylinder $G = 0$. At higher frequencies though, the same pattern as in Figure [3.4a] is observed. Similarly, the surge pitch added mass, Figure [3.4d], follows a similar rational, for greater values of G smaller values of A_{15} are noted. It is also noted that due to the body's symmetry $A_{15} = A_{51}$ which also holds true for this study.

Figure 3.5: Hydrodynamic damping B_{11} B_{33}, B_{55} B_{15} of the permeable cylindrical body against wave frequency ω for various values of porous effect parameter.

In Figure [3.5] the effect the porous coefficient has on the hydrodynamic damping of the porous cylindrical body, is shown. More specifically, in Figure [3.5a] one can notice that for lower frequencies $\omega < 0.5 \ rad/s$, B_{11} behaves proportionally, as the hydrodynamic damping increases as G does. However, for higher frequencies $\omega > 1.5 \ rad/s$ the behaviour reverses. Now, for higher values of G the local maxima of B_{11} are shifted to higher values. The same holds true for the cases of pitch hydrodynamic damping, as can be seen in Figure [3.5c] and of surge pitch hydrodynamic damping, Figure [3.5a]. Regarding, heave hydrodynamic damping B_{33}, as can be seen in Figure [3.5b], the same conclusions as in A_{33} variation can be drawn, as B_{33} decreases as G obtains larger values for small values of wave frequencies, and the increase of G tends to have no effect on B_{33} as frequency values get higher.

The effect the porous parameter G has on the permeable body's heave motion and on its response is shown in Figure [3.7]. The mass of the body is equal to $M = 3.62e^{-4}$t, regardless of the G value, since the porous sidewall is assumed to be infinitesimally thin and have negligible mass. The cases of the fully impermeable cylinder and of the fully submerged plate are not taken under consideration as they attain completely different hydrostatic coefficients.

Figure 3.6

Figure 3.7: Motion RAO_3 of the permeable cylindrical body against wave frequency ω for various values of porous effect parameter G

Regarding motion RAO_3, as can be seen in Figure [3.6] for ω tending to zero RAO_3 starts its variation from unity. However, as the G increases the permeable body's heave motion displacement decreases.

The following plots, Figure [3.8]-[3.11], show the effect of porous coefficient G on the hydrodynamic forces, moments and heave motion of the permeable cylindrical body, in various sea conditions. As can be seen in Figure [3.8], the surge hydrodynamic force, F_1, behaves reverse proportional to G. Furthermore, in every case of significant wave height H_s, F_1 decreases as peak wave period T_p obtains greater values and increases as significant wave height H_s does. Heave hydrodynamic force F_3, as seen in Figure [3.9, behaves reverse proportional to porous coefficient G. But, contrary to F_1, F_3 behaves proportional to peak wave period T_p, as well as to significant wave height H_s. Pitch hydrodynamic moment, F_5 as depicted in Figure [3.10] follows the same trend as F_1.

In Figure [3.11], the effect of porous coefficient G on the permeable cylindrical body's heave motion RAO_3 is depicted. RAO_3 obtains smaller values as G increases, though its effect becomes less significant as peak wave period T_p increases. Additionally, RAO_3 behaves proportional to both peak wave period T_p and significant wave height H_s.

23
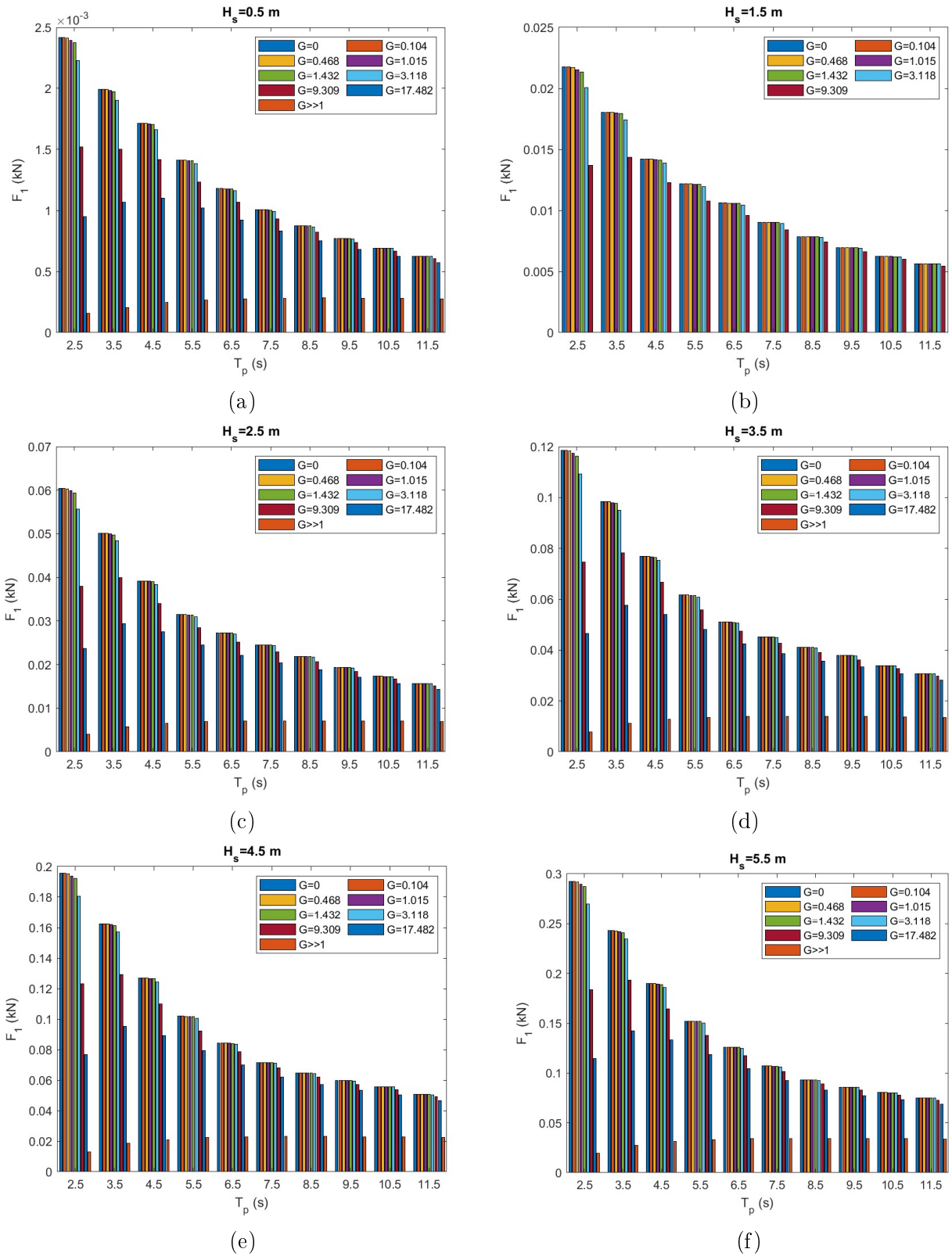
Figure 3.8: Values of F_1 against peak wave period T_p and significant wave height H_s for various values of porous effect parameter
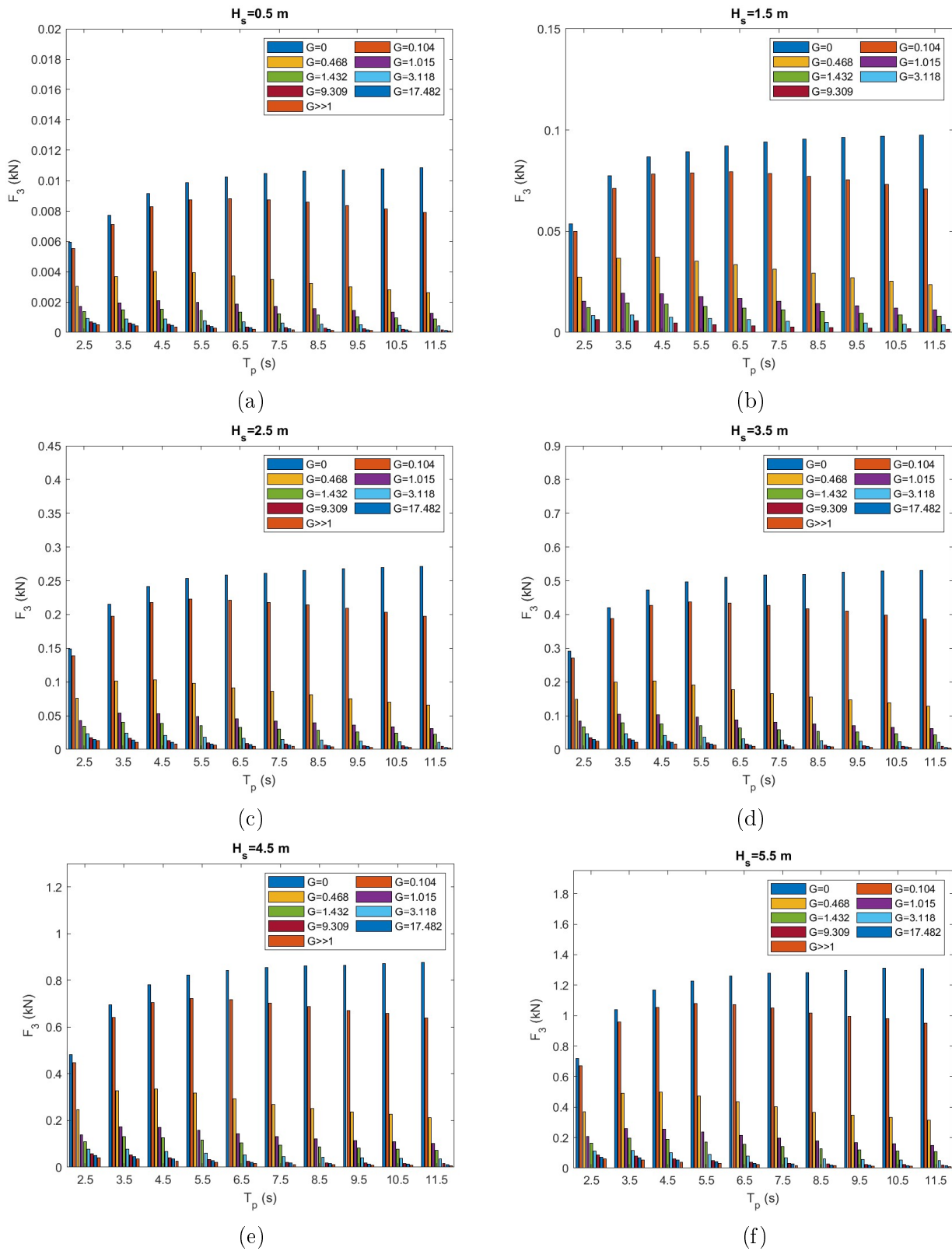
Figure 3.9: Values of F_3 against peak wave period T_p and significant wave height H_s for various values of porous effect parameter
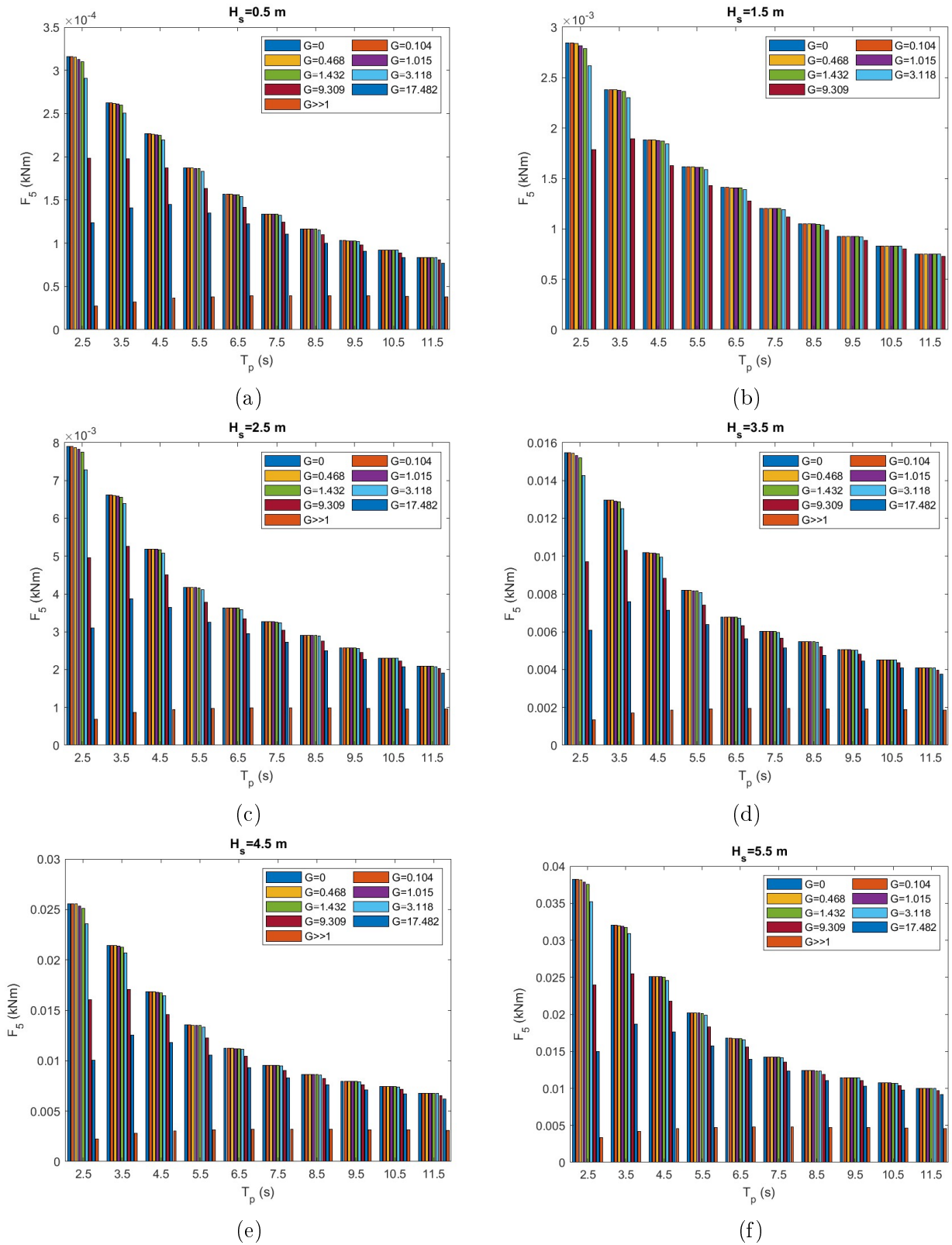
Figure 3.10: Values of F_5 against peak wave period T_p and significant wave height H_s for various values of porous effect parameter
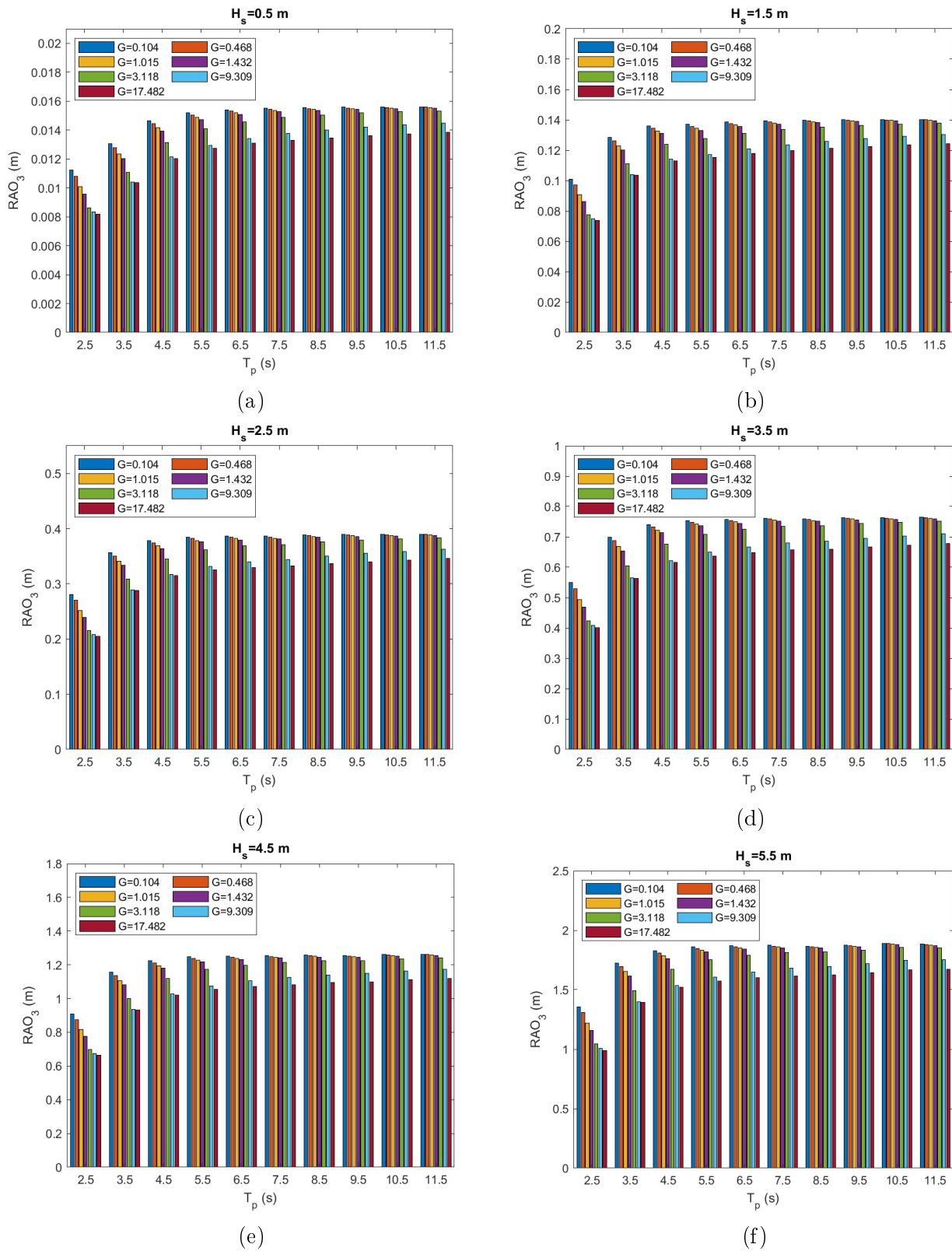
Figure 3.11: Values of RAO_3 against peak wave period T_p and significant wave height H_s for various values of porous effect parameter

3.2.2 Effect of the Radius

In this section, the effect the radius has on the hydrodynamic coefficients and exciting forces is examined. The body is, as aforementioned, a porous free floating cylinder of radius r, with an impermeable bottom of negligible thickness. It is subjected to waves propagating at zero angle in a constant water depth equal to $d = 5$ m. The circular frequency of the waves is denoted by ω with values ranging from $\omega = 0.05$ rad/s to $\omega = 3.0$ rad/s in steps of 0.05 rad/s. The characteristics, as in radius, mass, and mass moment of inertia relative to the free surface, of the examined test cases are seen below in 3. The center of gravity in all four cases is located in the vertical axis at $4.975\ m$ below the free surface, and the porous coefficient G is real and equal to $G = 1.432$.

	a	$2a$	$3a$	$4a$
$r\ (m)$	0.15	0.30	0.45	0.60
$M\ (t)$	$3.62 * 10^{-4}$	0.0014	0.0033	0.0058
$I_z\ (tm^2)$	$4.07 * 10^{-6}$	$6.52 * 10^{-4}$	$3.30 * 10^{-4}$	0.001

Table 3: Characteristics of Test Cases

(a)

(b)

(c)
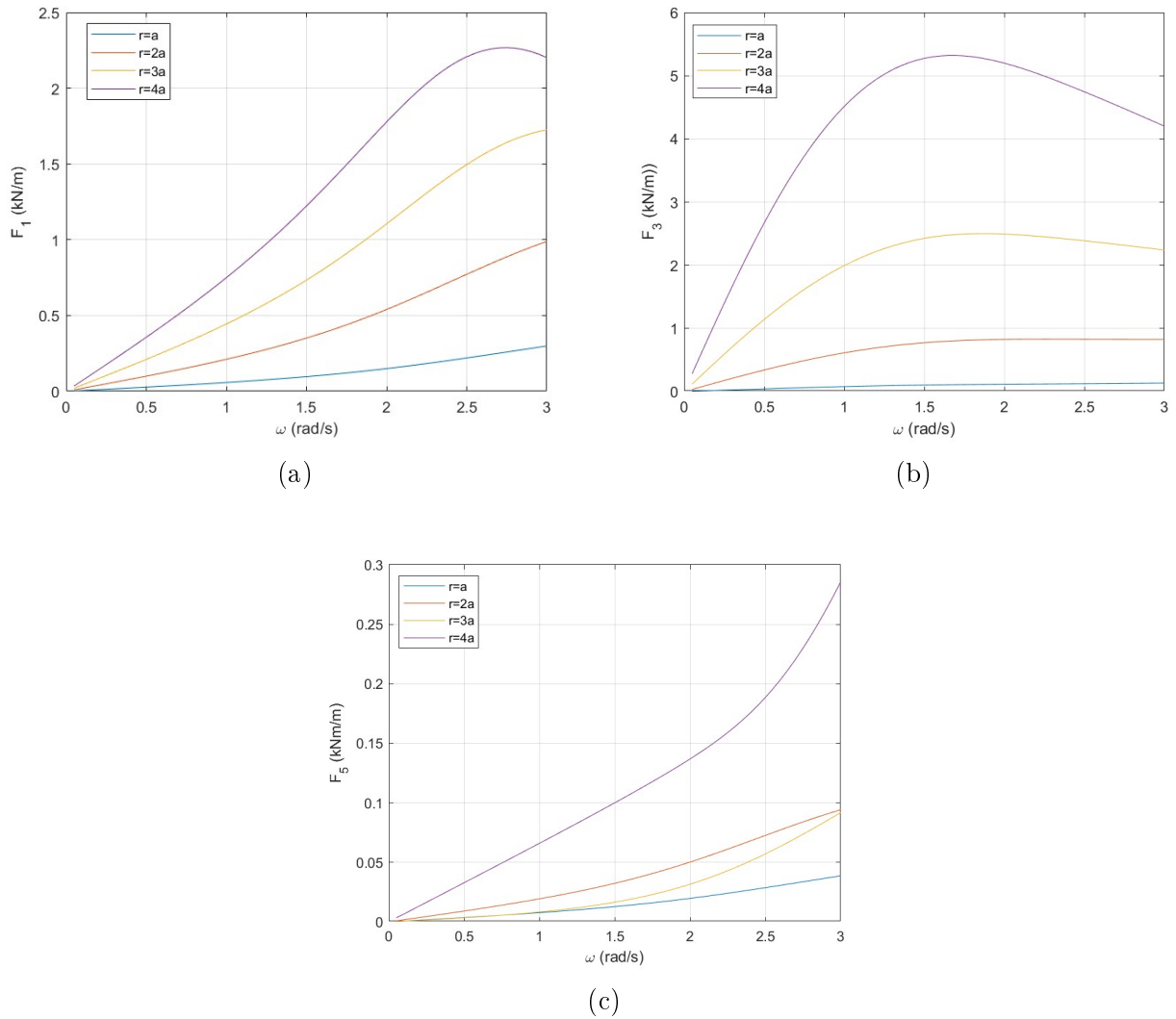
Figure 3.12: Exciting forces F_1, F_3 and moment F_5 on the permeable cylindrical body against wave frequency ω for various values of radius

The effect the value of the body's radius has on the exciting forces and overturning moment, is visualised in Figure [3.12]. Both surge F_1 and heave F_3 exciting forces, as seen in Figures [3.12a]-[3.12b], behave proportionally to radius values. It is also noted that in the case of heave,F_3, Figure [3.12b], the case of $r = 4a$ the curve corresponding to the $r = 4a$ case is characterised by a steeper slope and a rather larger local maximum in relation to the others. However, for the overturning moment, F_5, Figure [3.12c] the case is not the same. In the range of smaller frequencies $\omega < 1$ the case of the $r = 3a$ exhibits values close to $r = a$ case and as the frequencies increase it tends to meet the $r = 2a$ curve, while the $r = 4a$ curve continues to exhibit similar behaviour as in surge and heave, see Figures [3.12a]-[3.12b], with the main difference being that it exhibits maximum values at higher frequencies.
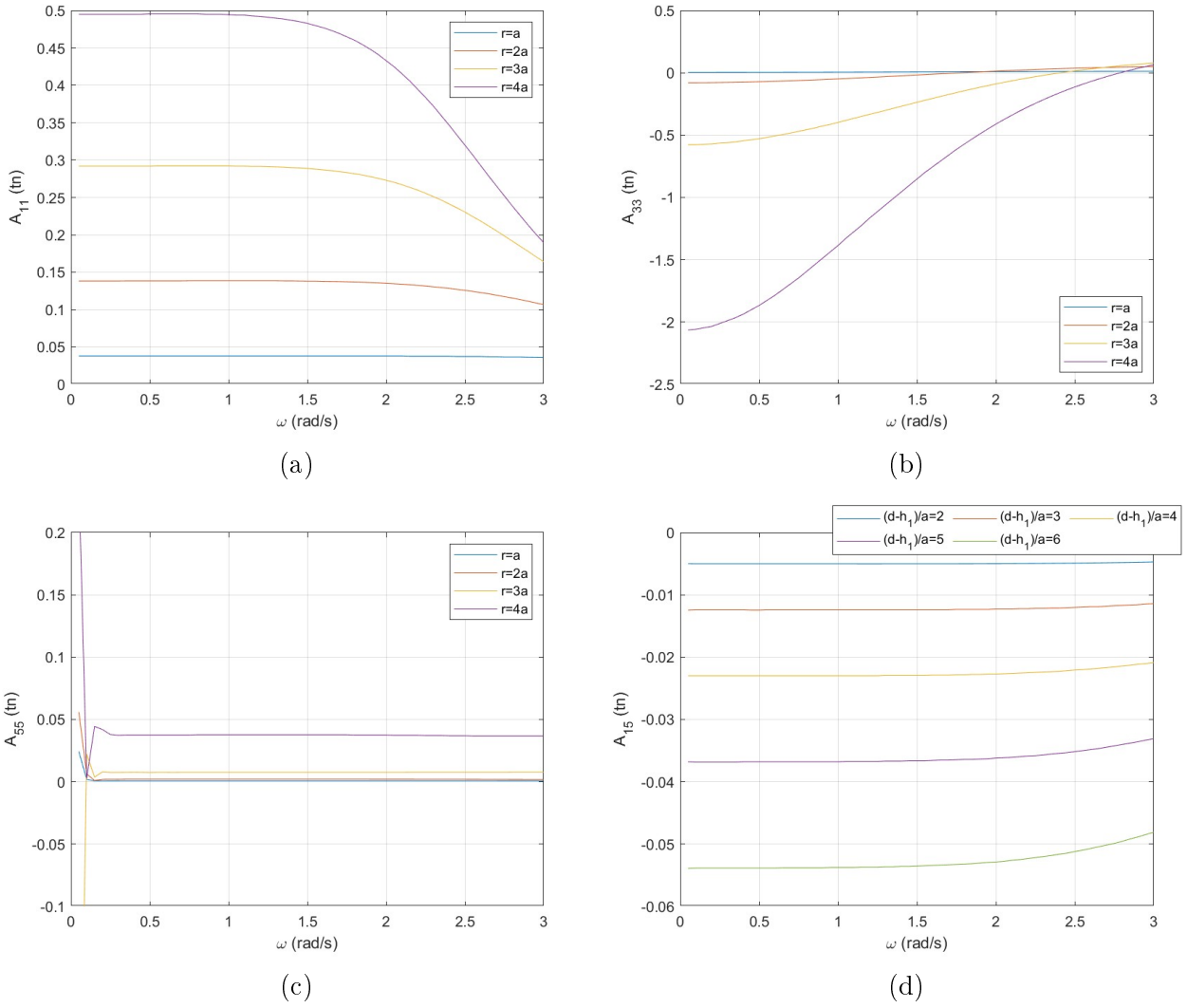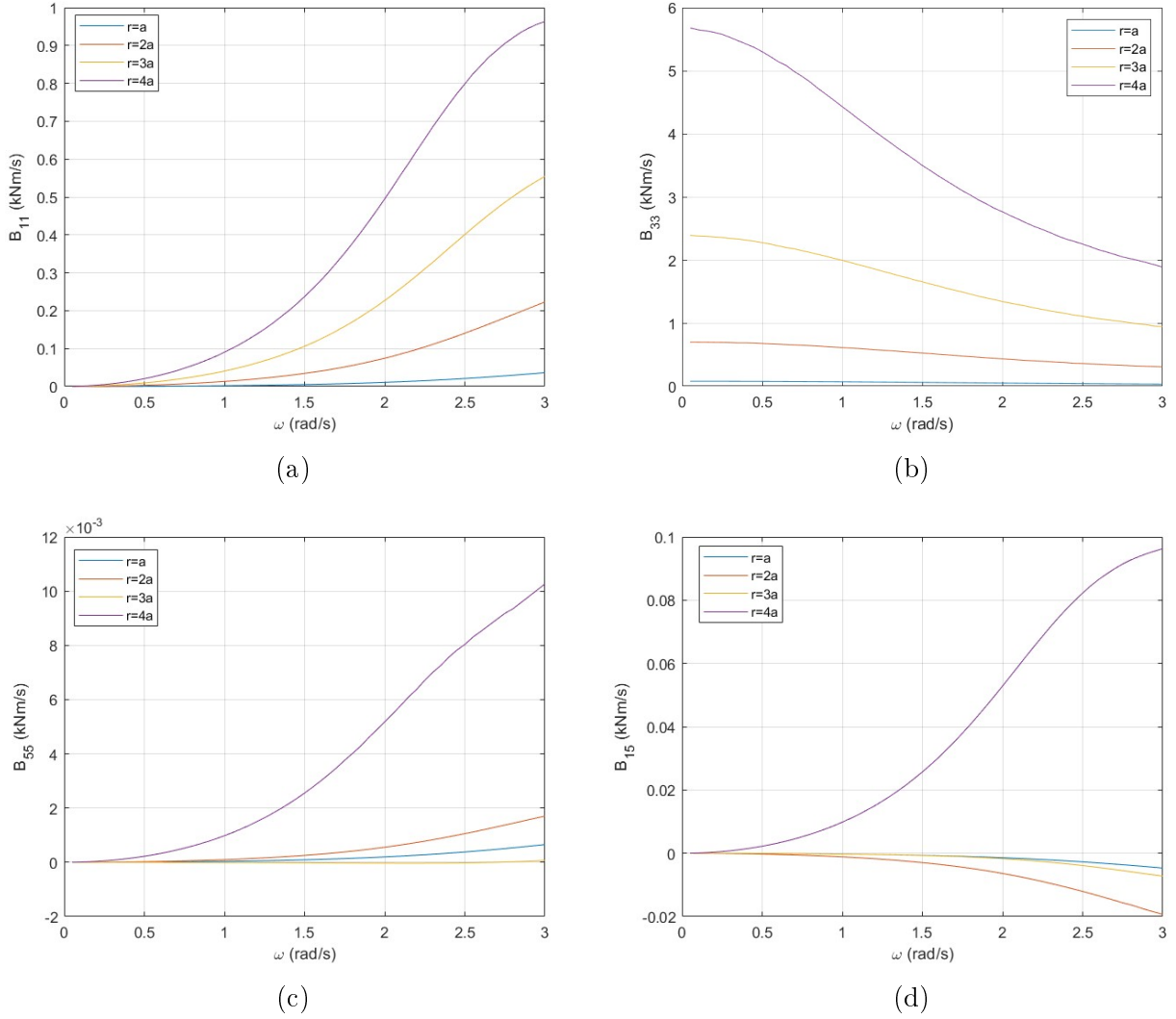
Figure 3.13: Hydrodynamic added mass A_{11} A_{33}, A_{55} A_{15} of the permeable cylindrical body against wave frequency ω for various values of radius.

Figure [3.13] depicts the hydrodynamic coefficient of added mass, of the examined permeable body, for various cases of radius value. Regarding the added mass in surge direction A_{11}, Figure [3.13a]], in the frequency range of $\omega < 1.5$ rad/s added mass is of proportionally greater value and constant for each case. As ω increases A_{11} tends to decrease, more rapidly so, for higher radius values. In Figure [3.13b] the added mass in heave direction, A_{33} is depicted. It can be seen that, A_{33} behaves reverse proportionally with r, as it decreases as r increases. This effect is more prominent for $\omega < 2.5 rad/s$ as for frequencies higher than that, A_{33} tends to zero in all the examined cases, making the effect of r negligible. The added mass in pitch direction A_{55}, is depicted on Figure [3.13c]. It can be noted, that the curves of $r = a$, $r = 2a$, $r = 4a$ attain a local maxima, that is of higher value for greater r values in the lower frequency range $\omega < 0.2$ rad/s whereas $r = 3a$ attains a local minima in the same range. For greater values of ω, A_{55} behaves proportionally with r. In case of surge pitch added mass A_{15}, Figure [3.13d], the curve corresponding to $r = 4a$ follows a similar behaviour as the one in surge, see Figure [3.13a], while it also holds true that for greater values of r, $A15$ increases as well, except for the case of $r = 2a$ which for the whole frequency range has a negative value of A_{15}. It also holds

true that $A_{15}=A_{51}$.

Figure 3.14: Hydrodynamic damping B_{11} B_{33}, B_{55} B_{15} of the permeable cylindrical body against wave frequency ω for various values of radius.

In Figure [3.14] the effect the value of the permeable cylindrical body's radius has on the hydrodynamic damping coefficient, against frequency, is depicted. The hydrodynamic damping coefficient in the surge direction B_{11}, Figure [3.14a], behaves proportionally with r, as r increases so does B_{11}, and this effect is more prominent as ω values get higher. In the range of $\omega < 0.3$ rad/s the effect of r is practically negligible. As can be seen in Figure [3.14b], the hydrodynamic damping in the heave direction B_{33}, behaves proportionally to r similarly with the case of B_{11}, see Figure [3.14a], with the key difference being, that in the case of B_{33} the effect of r is prominent in the whole frequency range. In the case of damping on the pitch direction B_{55}, Figure [3.14c], however, the aforementioned pattern is not followed. Here, the lowest values of B_{55} correspond to the case of $r = 3a$ presenting values near zero for frequencies smaller than $\omega < 1$ rad/s and attains negative values for the rest of the frequency range. Similarly, in the case of surge pitch damping B_{15} the case of $r = 4a$ exhibits a similar behaviour as in surge B_{11}, see Figure [3.14a], while the rest behave reverse proportionally and as r increases $B15$ attains

smaller values which for $\omega > 07 \ rad/s \ B_{15}$ are negative.
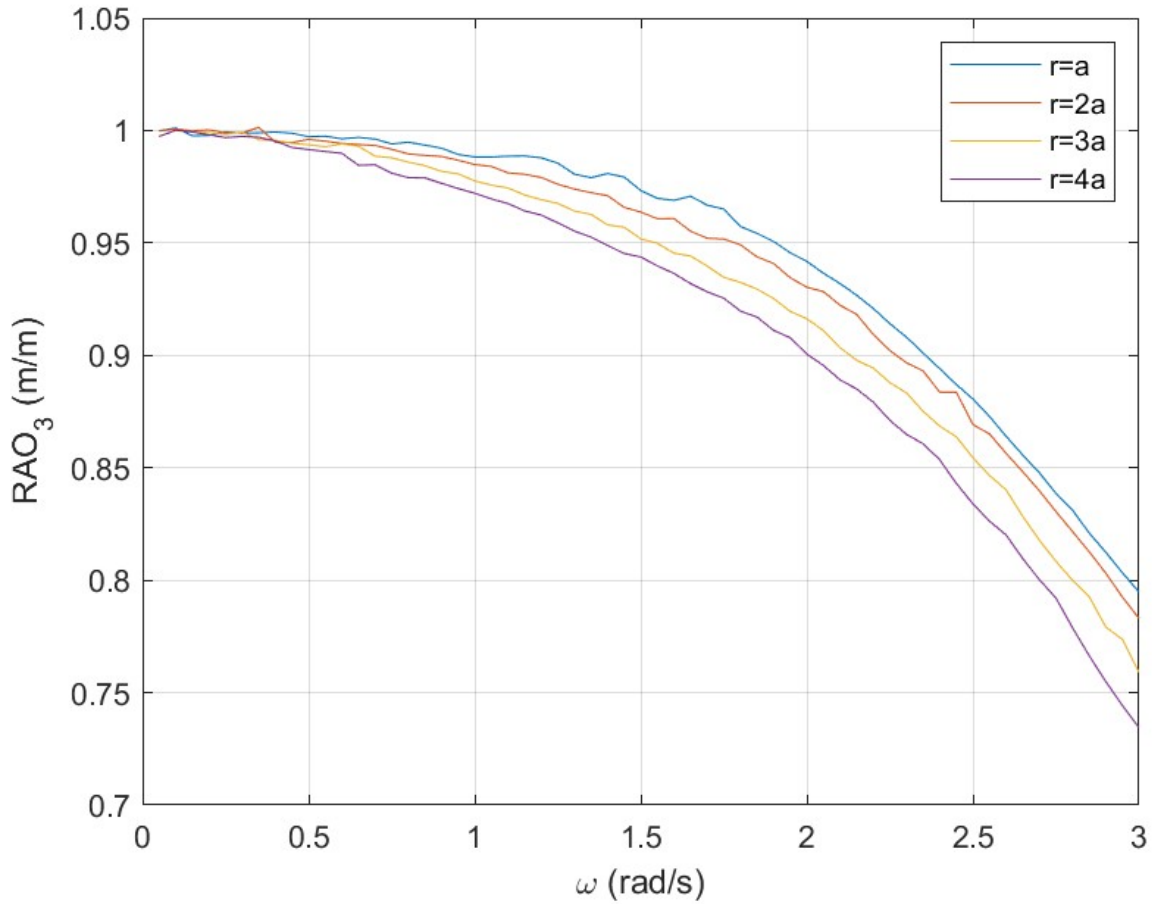
Figure 3.15

Figure 3.16: Motion RAO_3 of the permeable cylindrical body against wave frequency ω
against wave frequency ω for various values of radius

As it is shown in Figure [3.15] the heave motion RAO for ω tending to zero, starts its variation from unity. As ω increases, it is evident that for radius of greater values the heave motion displacement decreases.

The following plots, Figure [3.17]-[3.20], show the effect of radius on the hydrodynamic forces, moments and heave motion of the permeable cylindrical body, in various sea conditions. As can be seen in Figure [3.17], the surge hydrodynamic force, F_1, behaves proportional to radius. Furthermore, in every case of significant wave height H_s, F_1 increases until peak wave period obtains a value of $T_p = 2.5 \ s$ and then gradually decreases.
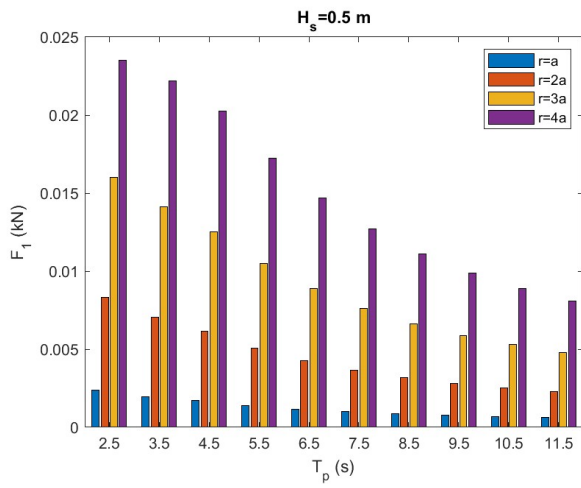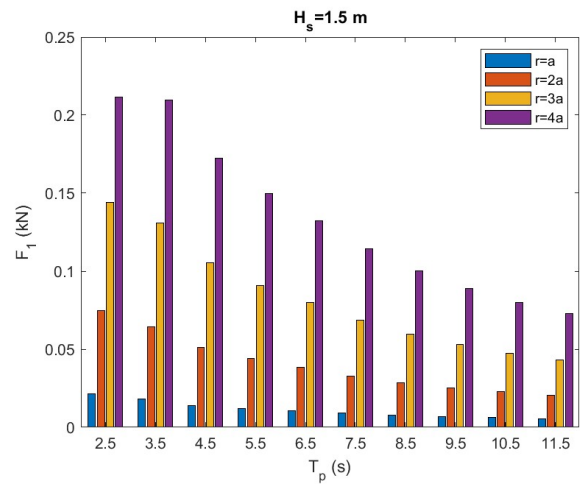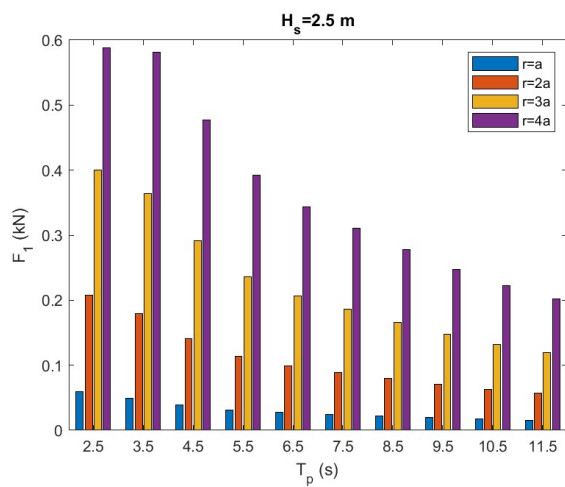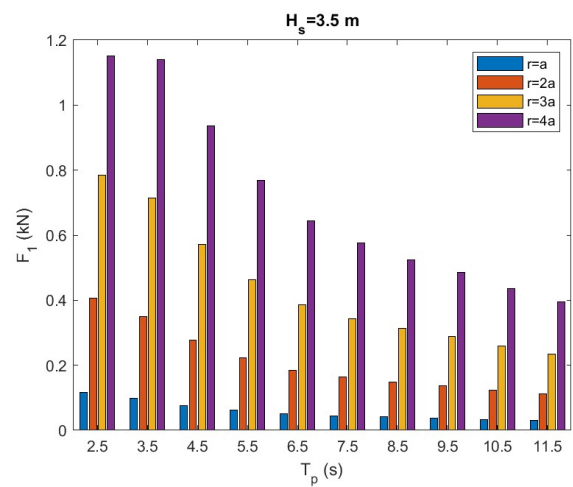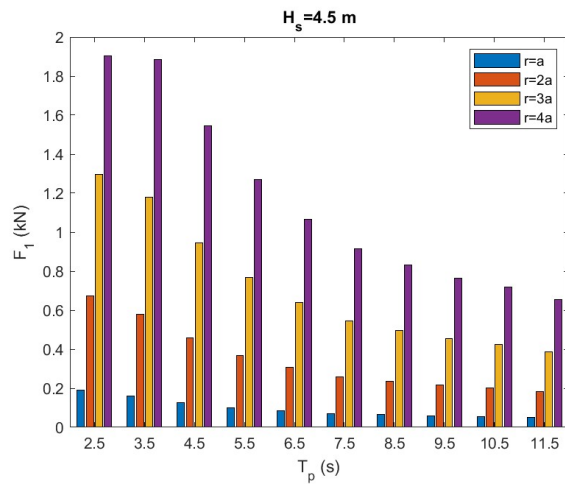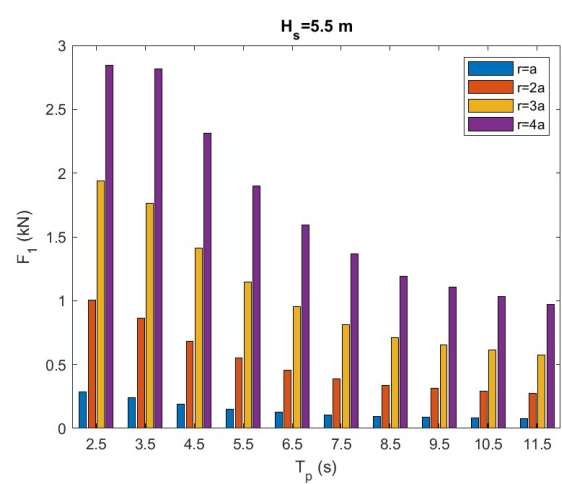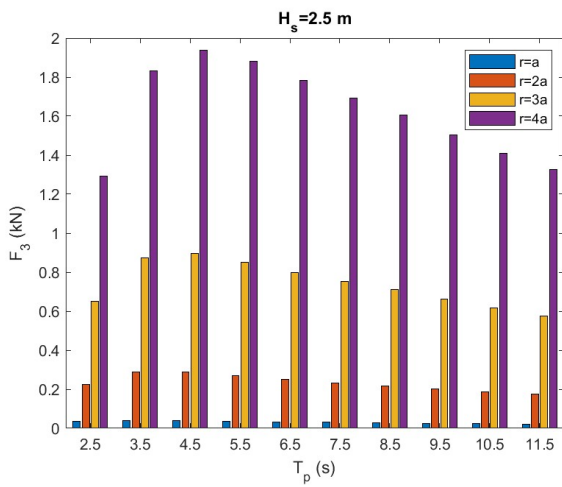
Figure 3.17: Values of F_1 against peak wave period T_p and significant wave height H_s for different values of radius
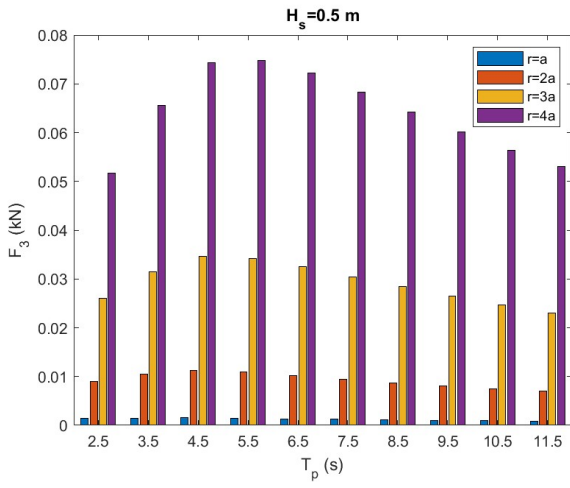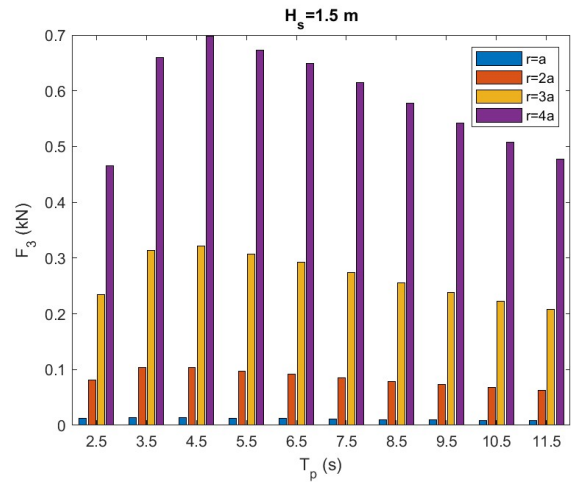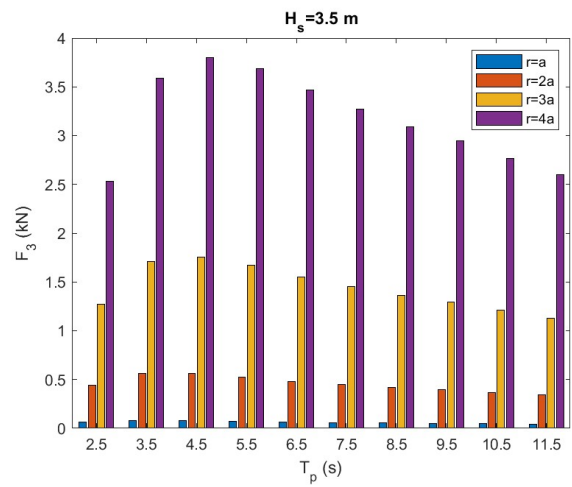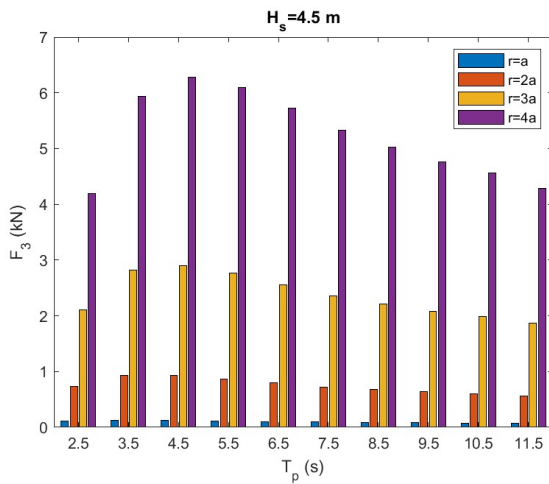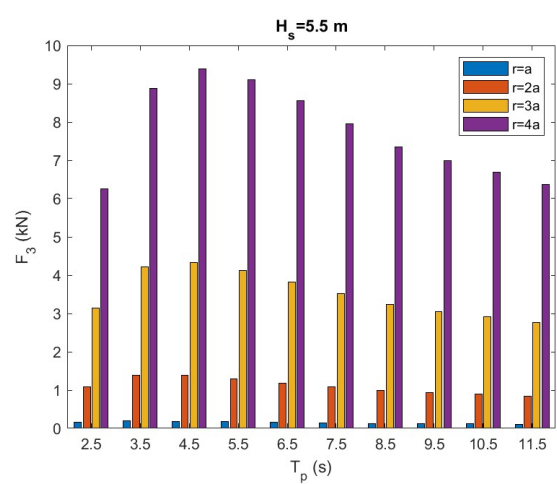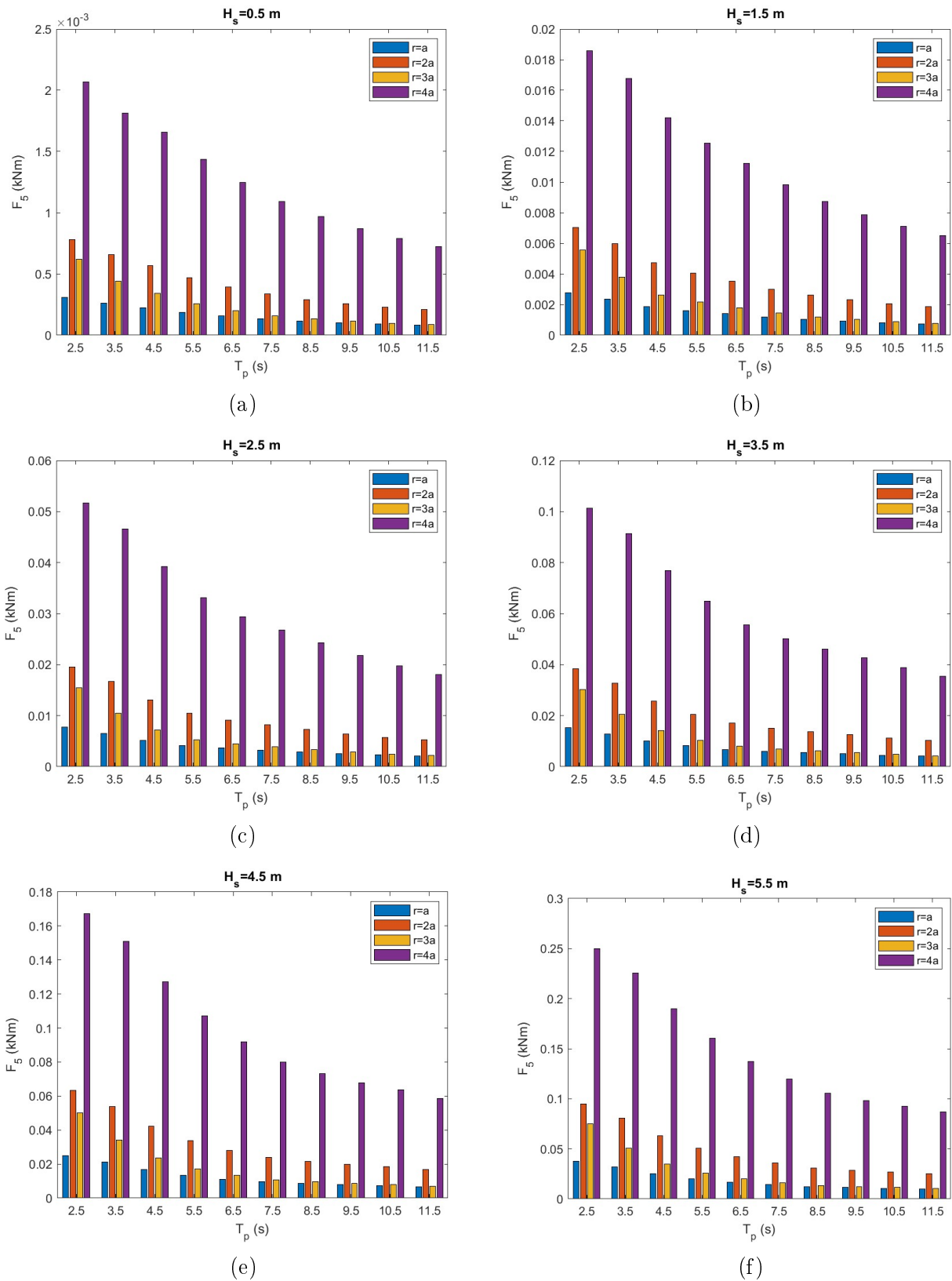
Figure 3.18: Values of F_3 against peak wave period T_p and significant wave height H_s for different values of radius

Figure 3.19: Values of F_5 against peak wave period T_p and significant wave height H_s for different values of radius
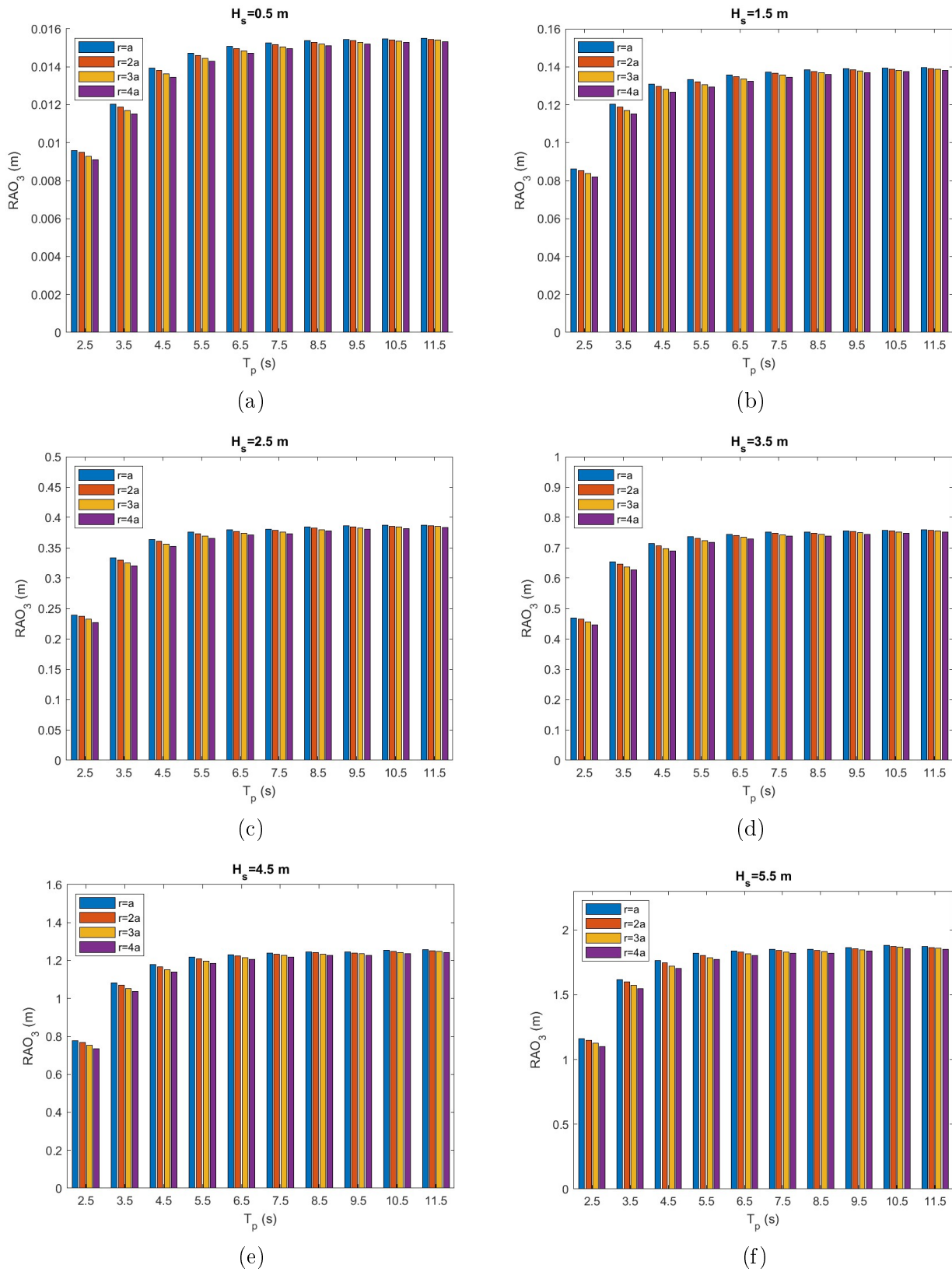
Figure 3.20: Values of RAO_3 against peak wave period T_p and significant wave height H_s for different values of radius

Heave hydrodynamic force F_3 as depicted in Figure [3.18], is also proportional to radius. In

most case of significant wave height, H_s, F_3 increases until peak wave period obtains a value of $T_p = 4.5\ s$ and then gradually decreases. In the case of $H_s = 0.5\ m$ the maximum value of F_3 corresponds to period of value $T_p = 5.5\ s$. As can be observed, in Figure [3.19], F_5 does not behave proportional to radius. In this case and in accordance to Figure [3.12], in case of $r = 2a$ hydrodynamic moment F_5 obtains greater values for every T_p, compared to $r = 3a$. Additionally, greater values F_5 correspond to lower values of peak wave period T_p.

In Figure [3.15], the effect of radius on the heave motion RAO_3 is shown. RAo_3 behaves reverse proportionally to radius, and as peak wave period obtains greater values the effect of radius becomes negligible.

3.2.3 Effect of Draught

In this section, the effect the draught has on the hydrodynamic coefficients and exciting forces is examined. The body is, as aforementioned, a porous free floating cylinder of radius r, with an impermeable bottom of negligible thickness. It is subjected to waves propagating at zero angle in a constant water depth equal to $d = 5$ m. The circular frequency of the waves is denoted by ω with values ranging from $\omega = 0.05$ rad/s to $\omega = 3.0$ rad/s in steps of 0.05 rad/s. The porous coefficient is real and equal to $G = 1.432$. The examined cases and the locations of corresponding center of gravity (CoG) at the vertical axis Z_G, of each case is shown below in Table (4).

$(d - h_1)/a$	2	3	4	5	6
$Z_G\ (m)$	4.697	4.547	4.397	4.247	4.097

Table 4: Examined cases of draught effect and location of center of gravity Z_G at the vertical axis

The effect the value of draught has on the body's exciting forces and moment is depicted in Figure [3.21]. Both surge F_1 exciting force and pitch F_5 moment , as seen in Figures [3.21a]-[3.21c] behave proportionally to the value of draught. As the draught increases so do the exciting force and moment. However, this is not the case for the heave exciting force F_3. In this case, as seen in Figure [3.21b], F_3 behaves reverse proportionally to the draught values. The effect of draught for the cases of $(d - h_1)/a = 4, 5, 6$ is more prominent in the frequency ranges of $\omega < 1.5\ rad/s$ and $\omega > 2\ rad/s$.
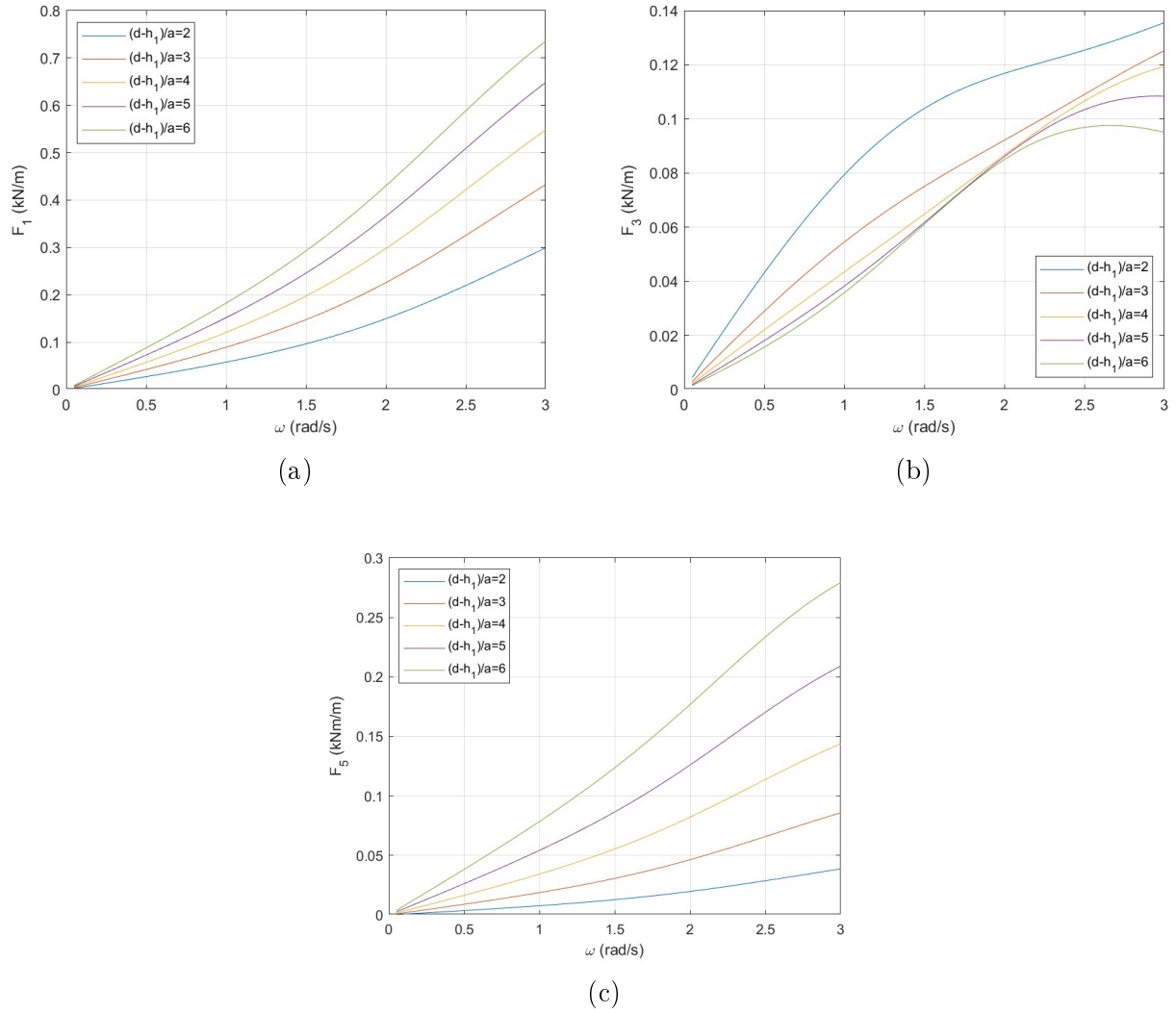
Figure 3.21: Exciting forces F_1, F_3 and moment F_5 on the permeable cylindrical body against wave frequency ω for various values of draught

The effect the draught has on the hydrodynamic added mass of the permeable body is depicted in Figure [3.22]. In the case of surge added mass A_{11} and surge pitch added mass A_{15}, Figure [3.22a] and Figure [3.22d] respectively, is clear that as the draught increases so does the added mass. The same holds true for the case of heave added mass A_{33} but in this case, as ω increases, the curves of A_{33} for different draught values tend to collide. In case of the pitch added mass A_{55}, Figure [3.22c] is worth noted that while in the cases of $(d-h1)/a = 2, 4, 6$ the corresponding added mass curves obtain local minima in the range of $\omega \simeq 0.1 rad/s$ the remaining cases of $(d-h1)/a = 3, 5$ obtain local maxima in the same frequency region.
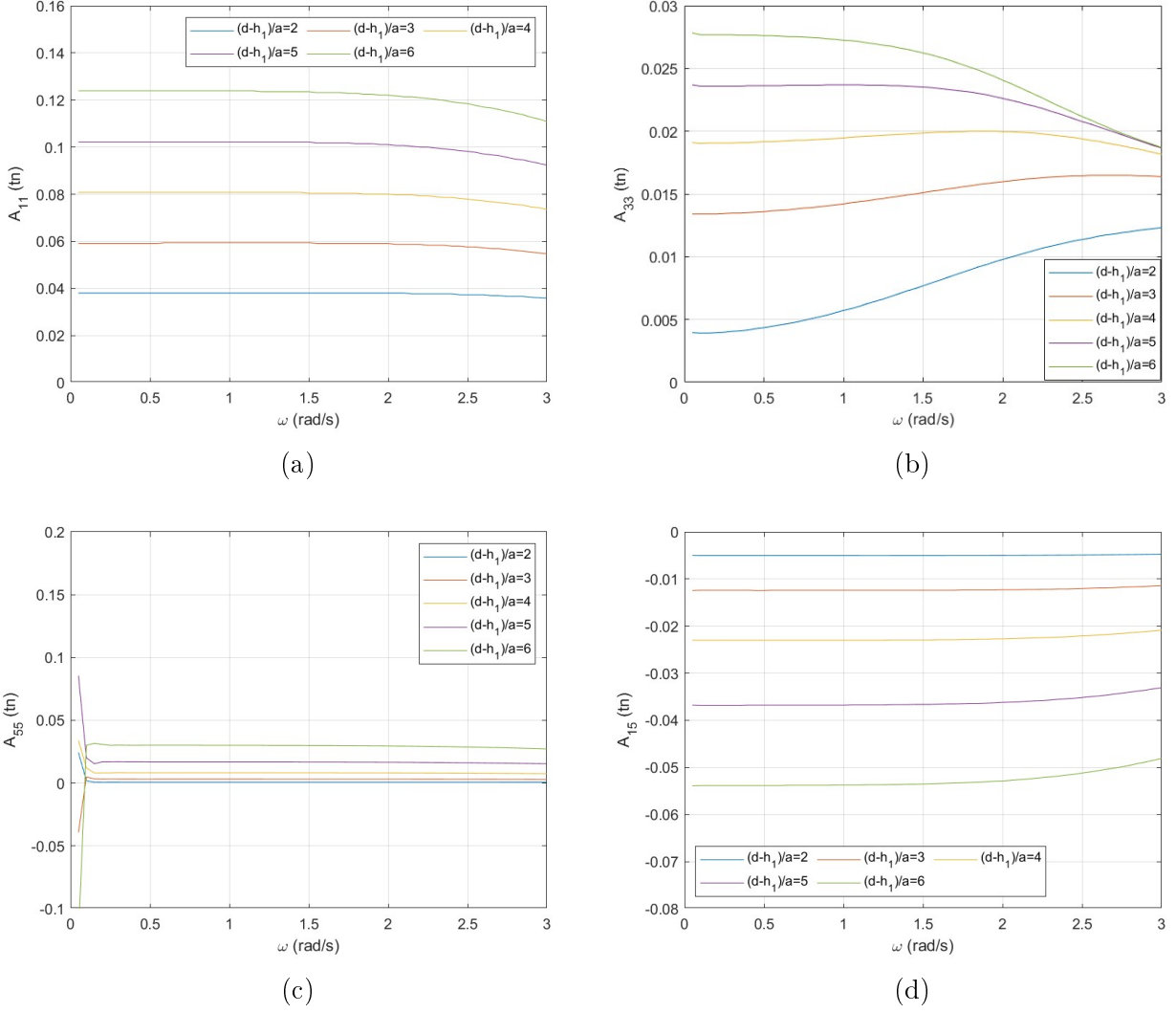
Figure 3.22: Hydrodynamic added mass A_{11} A_{33}, A_{55} A_{15} of the permeable cylindrical body against wave frequency ω for various values of draught.

In Figure [3.23] the effect the draught has, on the permeable cylindrical body's hydrodynamic damping coefficients, is depicted. In the cases of surge,B_{11}, pitch ,B_{55} and surge pitch B_{15}, Figures [3.23a],[3.23c] and [3.23d] respectively, the hydrodynamic damping coefficients exhibit the same behaviour. In the lower frequency range, $\omega < 0.5$ rad/s the value of draught has no significant impact on hydrodynamic damping, and as ω increases, the hydrodynamic damping coefficients behave proportionally to the draught, as the draught increases so does the hydrodynamic damping. This, however, is not the case for the heave hydrodynamic damping coefficient B_{33} as shown in Figure [3.23b]. In this case, for frequencies smaller than $\omega < 1.5$ rad/s B_{33} behaves reverse proportionally to draught, and for $\omega > 1.5$ rad/s the curve that corresponds to $(d - h_1)/a = 6$ follows an increasing trend whereas the rest of the cases exhibit a steady decline.
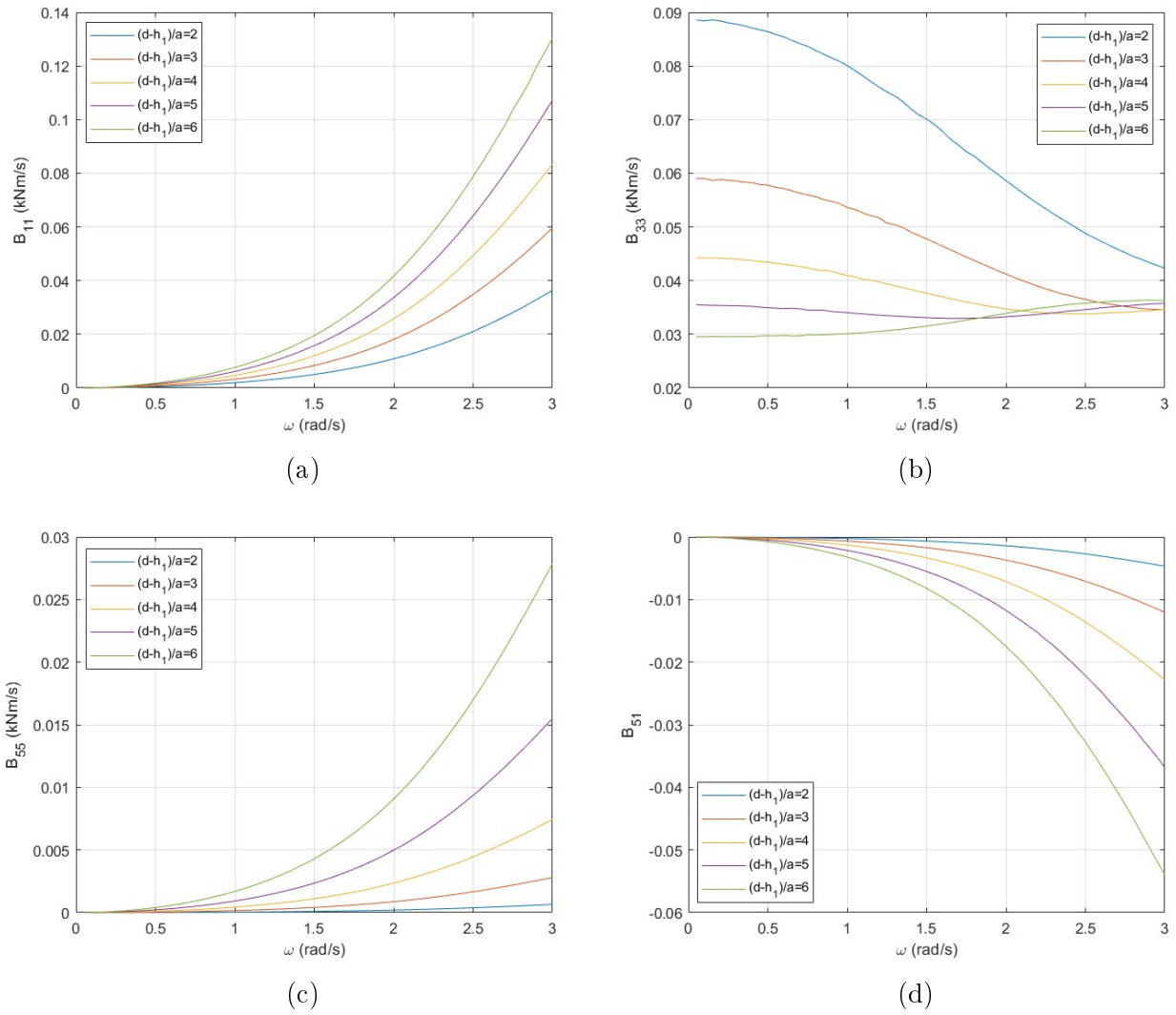
Figure 3.23: Hydrodynamic damping B_{11} B_{33}, B_{55} B_{15} of the permeable cylindrical body against wave frequency ω for various values draught.

In Figure [3.24], the effect different values of draught have on the permeable cylindrical body's heave motion RAO, is depicted. For ω tending zero, RAO_3 obtains a value of 1 for all the examined cases. As the ω increases, it is clear that for greater values of draught the heave motion displacement decreases.
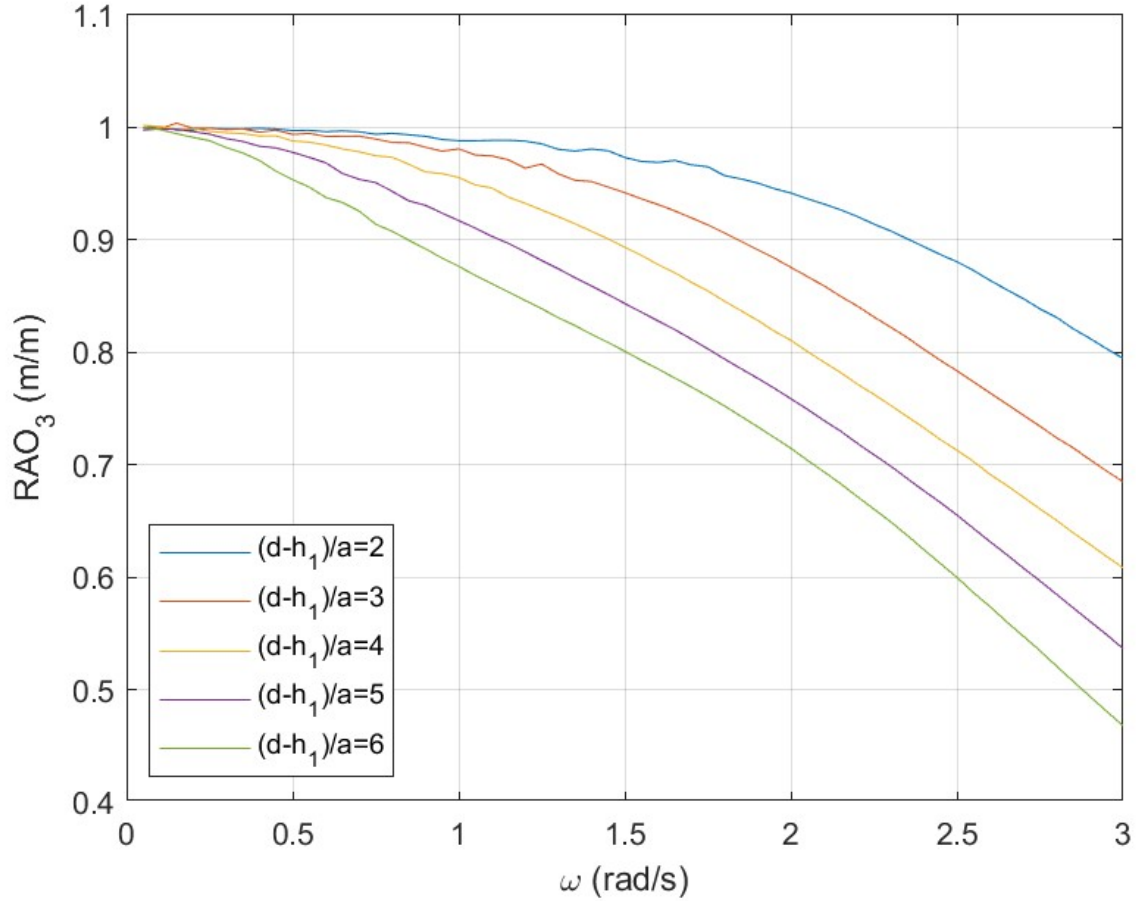
Figure 3.24

Figure 3.25: Motion RAO_3 of the permeable cylindrical body against wave frequency ω for various values of draught

The following plots, Figure [3.26]-[3.29], show the effect of draught on the hydrodynamic forces, moments and heave motion of the permeable cylindrical body, in various sea conditions. Regarding the hydrodynamic forces F_1 and F_5 Figures [3.26] and [3.28], it is evident that they behave proportional to the draught. It is also worth noted that the force and moment attain larger values as the significant wave height increases. Contrary, as the peak wave period increases, F_1 and F_5 decrease. In Figure [3.27] the effect of draught on heave force is depicted. In this case, the force behaves reverse proportional to the body, meaning that for higher values of draught, F_3 decreases. The peak values of heave F_3 in most sea states, are obtained for values of peak wave period $T_p \simeq 3.5\ s$. The exception being the case of $H_s 0.5\ m$, Figure [3.29] where F_3 obtains peak values for peak wave period of $T_p = 4.5\ s$.

Regarding heave motion RAO_3, as it is shown in Figure [3.29], it also behaves proportional to draught. The higher values of RAO_3 are obtained for the extreme weather conditions of $H_s = 5.5\ m$ and $T_p = 11.5\ s$. It is also worth noted, that draught seems to have less effect on RAO_3 as T_p increases.
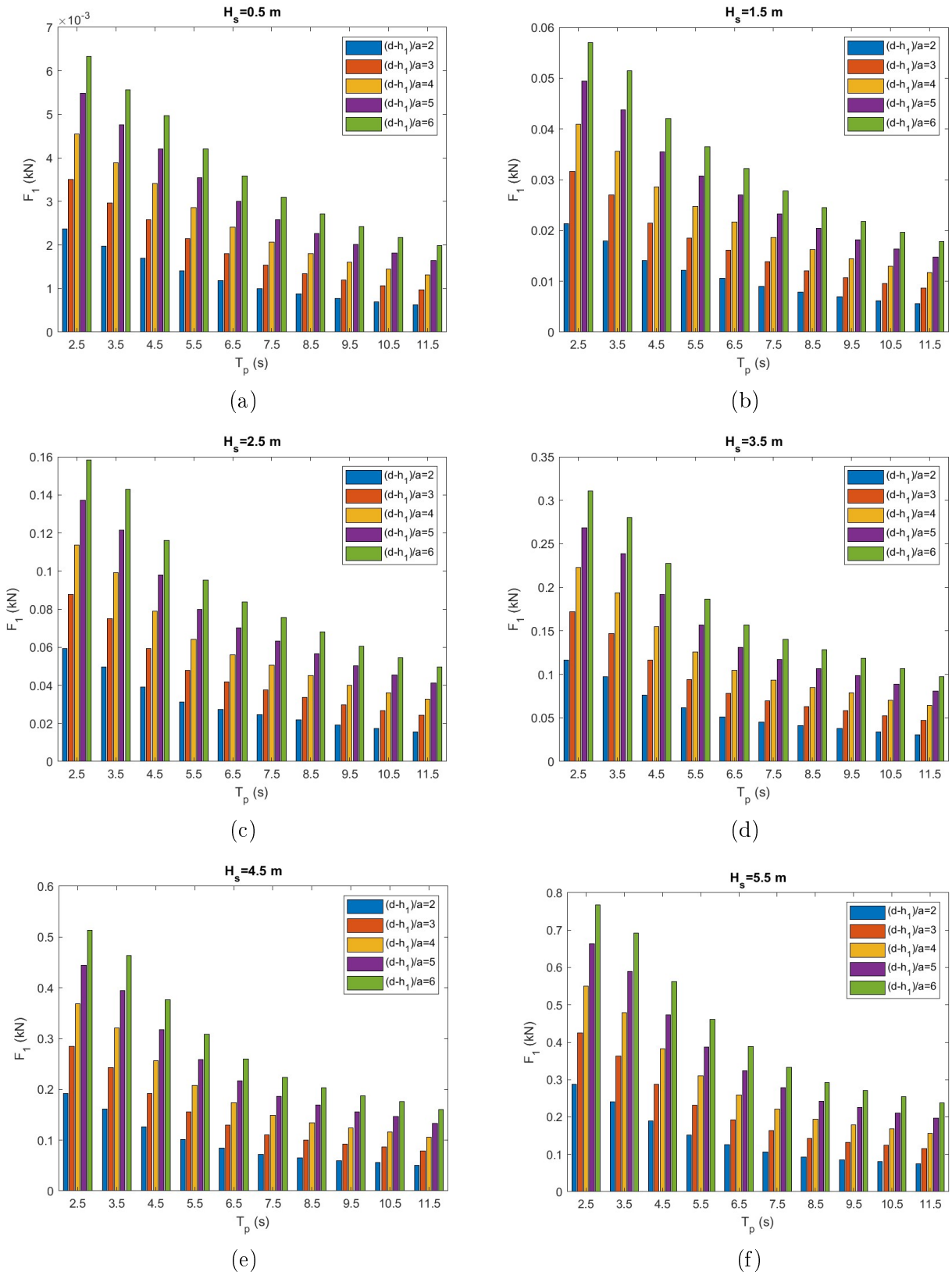
Figure 3.26: Values of F_1 against peak wave period T_p and significant wave height H_s for various values of draught
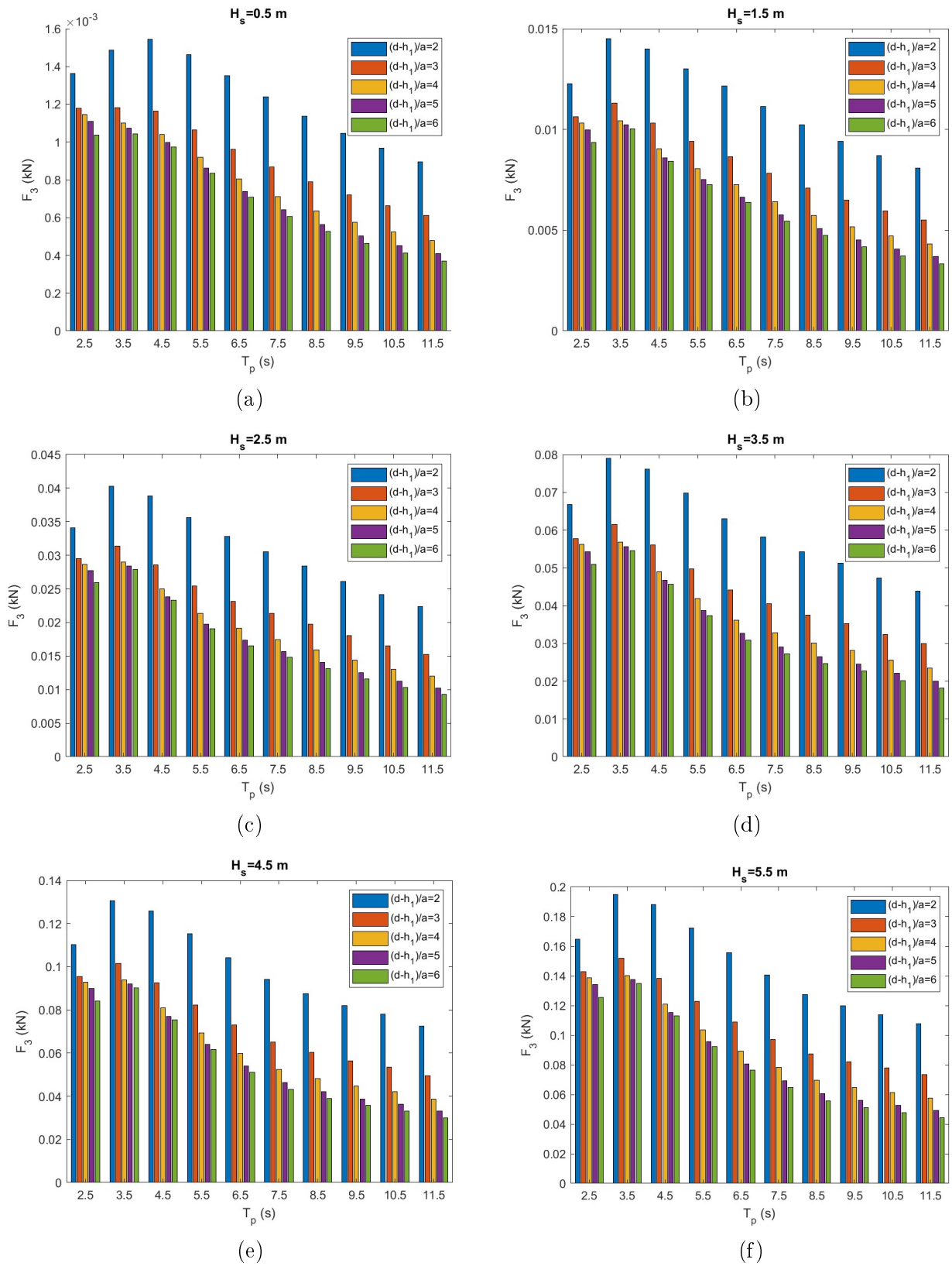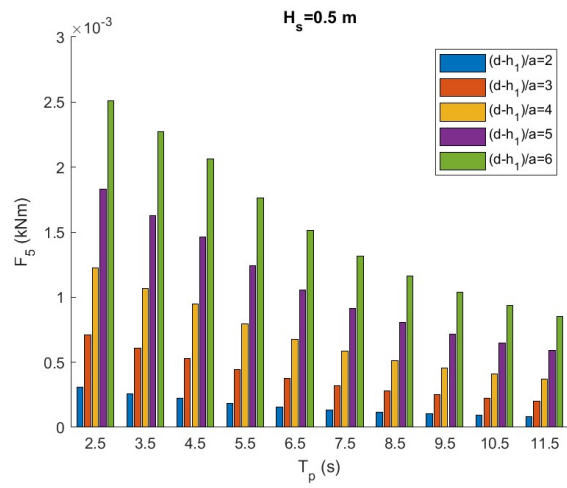
Figure 3.27: Values of F_3 against peak wave period T_p and significant wave height H_s for various values of draught

Figure 3.28: Values of F_5 against peak wave period T_p and significant wave height H_s for various values of draught
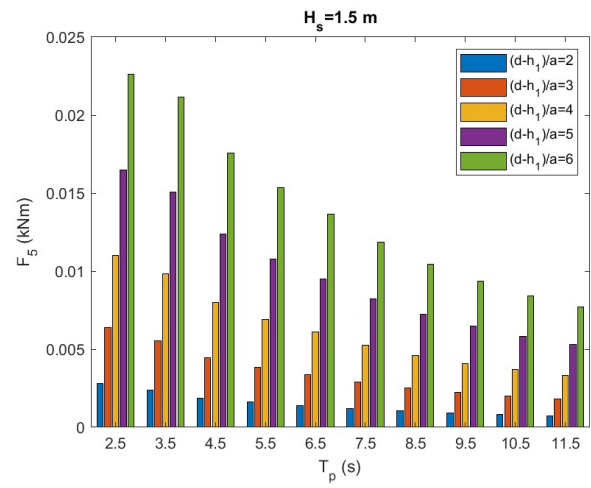
Figure 3.29: Values of RAO_3 against peak wave period T_p and significant wave height H_s for various values of draught

4 Conclusions and Future Work
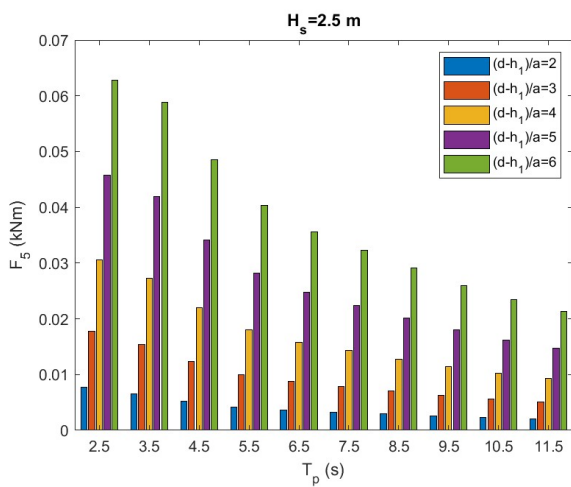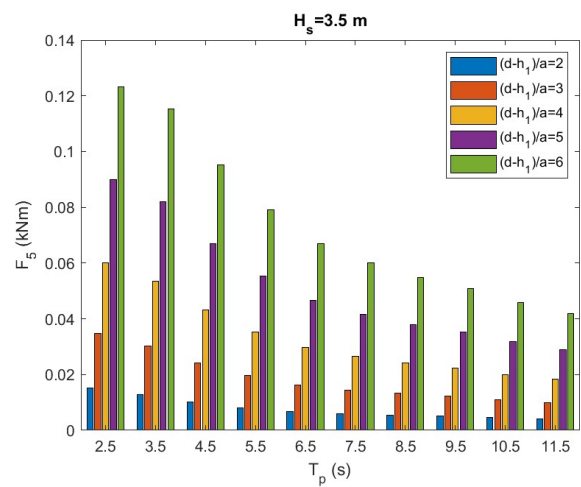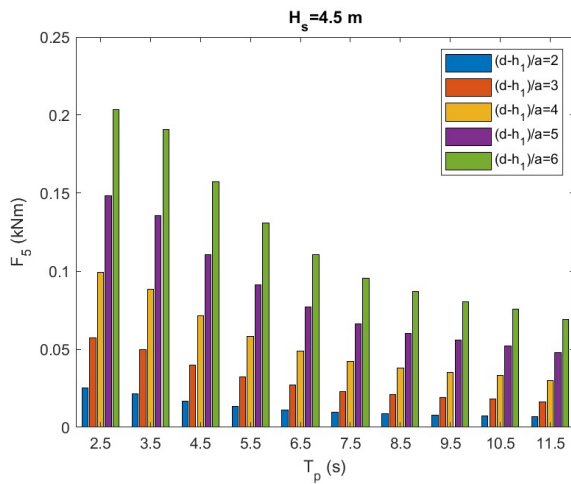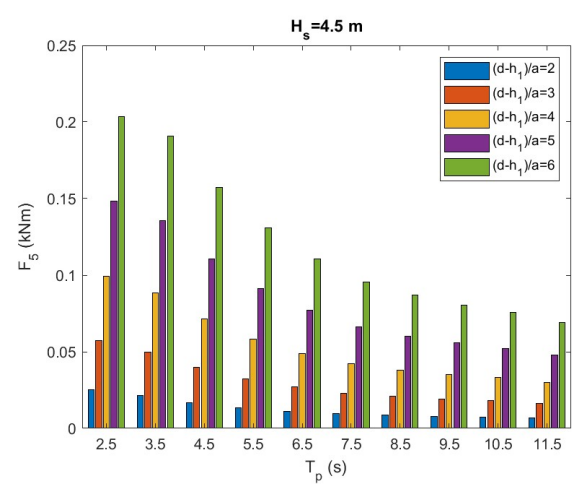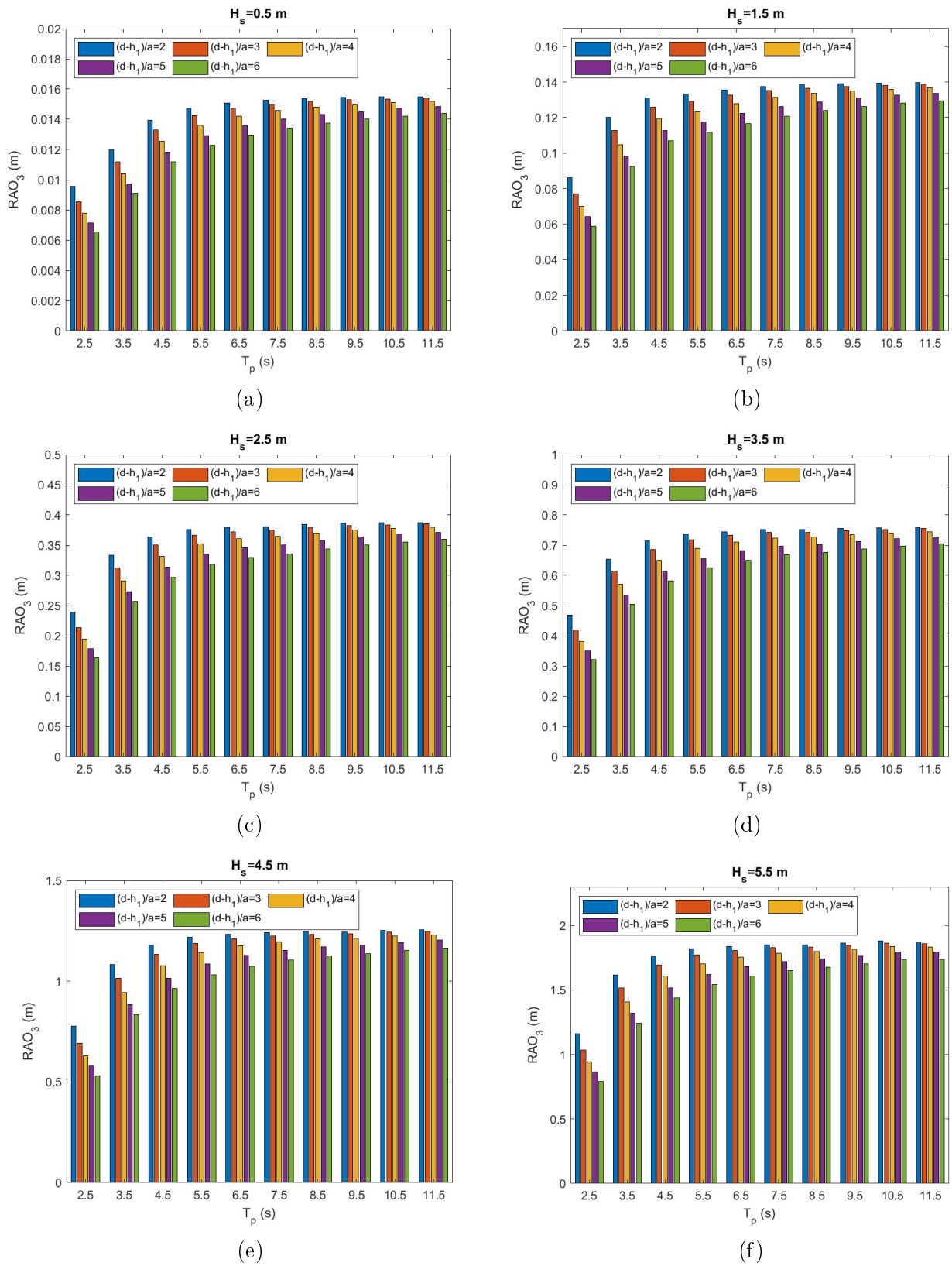
In the present a study a free floating, permeable cylinder body in the presence of regular waves was investigated. In order to investigate the hydrodynamics of the body, and within the realm of the linear theory, a three dimensional theoretical solution based on the eigenfunction method was developed for the determination of the velocity potential of the flow field around the cylindrical body. Furthermore, the linear resistance law was implemented to connect the the pressure drop across the porous boundary to normal velocity. The main conclusions drawn from this study are:

- The porous boundary contributes to the presence of reduced hydrodynamic forces and moment compared to those of the solid cylinder.

- The value of porous coefficient G plays a key role in the hydrodynamic forces and moment acting on the body as they decrease proportionally with its increase.

- The value of porous coefficient G is significant in the body's heave motion RAO as well as in its response in real waves.

- The overturning moment F_5 increases proportionally with the body radius for all cases except $r = 2a$, this occurs due to the low damping values B_{55} for the case of $r = 2a$ leading to higher values of exciting moment.

This research can by further expanded by taking into account the wave interaction between arrays of floating porous bodies. Additionally, it can be further developed in order to study floating porous bodies with flexible sidewalls, in order to simulate fish cages.

References

[1] Kwangho Lee, Ju Bae, Sang-Gi Kim, and Kim do Sam. Three-dimensional simulation of wave reflection and pressure acting on circular perforated caisson breakwater by olafoam. *Journal of Korean Society of Coastal and Ocean Engineers*, 29:286–304, 12 2017.

[2] Zhenhua Huang, Yucheng Li, and Yong Liu. Hydraulic performance and wave loadings of perforated/slotted coastal structures: A review. *Ocean Engineering*, 38(10):1031–1053, 2011.

[3] Jarlan G.E. A perforated vertical wall breakwater. *Dock and Harbour Authority XII*, 486:394–398, 1961.

[4] JS Mani and S Jayakumar. Wave transmission by suspended pipe breakwater. *Journal of Waterway, Port, Coastal and Ocean Engineering*, 121(6):335–338, 1995.

[5] Alireza Valizadeh, Ashkan Rafiee, Vivek Francis, Murray Rudman, and Balaji Ramakrishnan. An analysis of perforated plate breakwaters. In *The 28th International Ocean and Polar Engineering Conference*. OnePetro, 2018.

[6] Sunny Kumar Poguluri and IH Cho. Analytical and numerical study of wave interaction with a vertical slotted barrier. *Ships and Offshore Structures*, 16(9):1012–1024, 2021.

[7] Takeshi Ijima, Chung Ren Chou, and Akinori Yoshida. Method of analyses for two-dimensional water wave problems. In *Coastal Engineering 1976*, pages 2717–2736. 1977.

[8] Ed Mackay and Lars Johanning. Comparison of analytical and numerical solutions for wave interaction with a vertical porous barrier. *Ocean Engineering*, 199:107032, 2020.

[9] Charles K Sollitt and Ralph H Cross. Wave transmission through permeable breakwaters. In *Coastal engineering 1972*, pages 1827–1846. 1973.

[10] W Sulisz. Wave reflection and transmission at permeable breakwaters of arbitrary cross-section. *Coastal Engineering*, 9(4):371–386, 1985.

[11] MKM Darwiche, AN Williams, and K-H Wang. Wave interaction with semiporous cylindrical breakwater. *Journal of waterway, port, coastal, and ocean engineering*, 120(4):382–403, 1994.

[12] IJ Losada, MA Losada, and FL Martin. Experimental study of wave-induced flow in a porous structure. *Coastal Engineering*, 26(1-2):77–98, 1995.

[13] Eric Joseph Pereira, Hee Min Teh, Lachmi Sri Manoharan, and Chai Heng Lim. Design optimization of a porous box-type breakwater subjected to regular waves. In *MATEC Web of Conferences*, volume 203, page 01018. EDP Sciences, 2018.

[14] SW Twu and DT Lin. On a highly effective wave absorber. *Coastal Engineering*, 15(4):389–405, 1991.

[15] B Molin and JM Fourest. Numerical modeling of progressive wave absorbers. In *Proc. 7th Int*, 1992.

[16] Allen T Chwang. A porous-wavemaker theory. *Journal of Fluid Mechanics*, 132:395–406, 1983.

[17] AT Chwang and W Li. A piston-type porous wavemaker theory. *Journal of Engineering Mathematics*, 17(4):301–313, 1983.

[18] AT Chwang and Z Dong. Wave-trapping due to a porous plate. In *Proceedings of the 15th ONR Symposium on Naval Hydrodynamics*, pages 407–414, 1984.

[19] Harekrushna Behera and Trilochan Sahoo. Hydroelastic analysis of gravity wave interaction with submerged horizontal flexible porous plate. *Journal of Fluids and Structures*, 54:643–660, 2015.

[20] S Zheng, MH Meylan, D Greaves, and Gregorio Iglesias. Water-wave interaction with submerged porous elastic disks. *Physics of Fluids*, 32(4):047106, 2020.

[21] S.C. Mohapatra and C. Guedes Soares. Hydroelastic behaviour of a submerged horizontal flexible porous structure in three-dimensions. *Journal of Fluids and Structures*, 104:103319, 2021.

[22] Sarat Chandra Mohapatra and C. Guedes Soares. Hydroelastic response of a flexible submerged porous plate for wave energy absorption. *Journal of Marine Science and Engineering*, 8(9), 2020.

[23] Keh-Han Wang and Xugui Ren. Wave interaction with a concentric porous cylinder system. *Ocean Engineering*, 21(4):343–360, 1994.

[24] G Govaere, R Silva, and JA Maza. Wave kinematics around a protected cylindrical impermeable pile. In *Proc Coastal Structures99 Conf*, volume 1, pages 151–158, 1999.

[25] AN Williams and W Li. Water wave interaction with an array of bottom-mounted surface-piercing porous cylinders. *Ocean Engineering*, 27(8):841–866, 2000.

[26] AN Williams, W Li, and K-H Wang. Water wave interaction with a floating porous cylinder. *Ocean Engineering*, 27(1):1–28, 2000.

[27] B Teng, M Zhao, and Y Li. Wave diffraction from a cylinder with porous upper wall and an inner column. *Acta Oceanologica Sinica*, 23(6), 2001.

[28] K Sankarbabu, SA Sannasiraj, and V Sundar. Interaction of regular waves with a group of dual porous circular cylinders. *Applied Ocean Research*, 29(4):180–190, 2007.

[29] K Vijayalakshmi, R Sundaravadivelu, K Murali, and S Neelamani. Hydrodynamics of a concentric twin perforated circular cylinder system. *Journal of waterway, port, coastal, and ocean engineering*, 134(3):166–177, 2008.

[30] W Bao, T Kinoshita, and F Zhao. Wave forces acting on a semi-submerged porous circular cylinder. *Proceedings of the Institution of Mechanical Engineers, Part M: Journal of Engineering for the Maritime Environment*, 223(3):349–360, 2009.

[31] Min-Su Park, Weoncheol Koo, and Yoonrak Choi. Hydrodynamic interaction with an array of porous circular cylinders. *International Journal of Naval Architecture and Ocean Engineering*, 2(3):146–154, 2010.

[32] Fenfang Zhao, Weiguang Bao, Takeshi Kinoshita, and Hiroshi Itakura. Theoretical and experimental study on a porous cylinder floating in waves. *Journal of offshore mechanics and Arctic engineering*, 133(1), 2011.

[33] Fen-fang Zhao, Takeshi Kinoshita, Wei-guang Bao, Liu-yi Huang, Zhen-lin Liang, and Rong Wan. Interaction between waves and an array of floating porous circular cylinders. *China Ocean Engineering*, 26(3):397–412, 2012.

[34] Min-Su Park and Weoncheol Koo. Mathematical modeling of partial-porous circular cylinders with water waves. *Mathematical Problems in Engineering*, 2015, 2015.

[35] De-Zhi Ning, Xuan-Lie Zhao, Bin Teng, and Lars Johanning. Wave diffraction from a truncated cylinder with an upper porous sidewall and an inner column. *Ocean Engineering*, 130:471–481, 2017.

[36] Jørgen Dokken, John Grue, and Lars Petter Karstensen. Wave analysis of porous geometry with linear resistance law. *Journal of Marine Science and Application*, 16(4):480–489, 2017.

[37] Jørgen S Dokken, John Grue, and Lars P Karstensen. Wave forces on porous geometries with linear and quadratic pressure-velocity relations. In *32nd International Workshop on Water Waves and Floating Bodies, Dalian, China*, 2017.

[38] Peiwen Cong, Wei Bai, and Bin Teng. Analytical modeling of water wave interaction with a bottom-mounted surface-piercing porous cylinder in front of a vertical wall. *Journal of Fluids and Structures*, 88:292–314, 2019.

[39] Dimitrios N Konispoliatis, Ioannis K Chatjigeorgiou, and Spyros A Mavrakos. Hydrodynamics of a moored permeable vertical cylindrical body. *Journal of Marine Science and Engineering*, 10(3):403, 2022.

[40] Li Li, Shixiao Fu, Yuwang Xu, Jungao Wang, and Jianmin Yang. Dynamic responses of floating fish cage in waves and current. *Ocean Engineering*, 72:297–303, 2013.

[41] Zhongchi Liu, Sarat Chandra Mohapatra, and C Guedes Soares. Finite element analysis of the effect of currents on the dynamics of a moored flexible cylindrical net cage. *Journal of Marine Science and Engineering*, 9(2):159, 2021.

[42] Odd M Faltinsen. Hydronamic aspects of a floating fish farm with circular collar. 2011.

[43] Trygve Kristiansen and Odd M Faltinsen. Modelling of current loads on aquaculture net cages. *Journal of Fluids and Structures*, 34:218–235, 2012.

[44] Trygve Kristiansen and Odd M Faltinsen. Experimental and numerical study of an aquaculture net cage with floater in waves and current. *Journal of Fluids and Structures*, 54:1–26, 2015.

[45] Yugao Shen, Marilena Greco, Odd M Faltinsen, and Ivar Nygaard. Numerical and experimental investigations on mooring loads of a marine fish farm in waves and current. *Journal of Fluids and Structures*, 79:115–136, 2018.

[46] Sho Ito, Takeshi Kinoshia, and Weiguang Bao. Hydrodynamic behaviors of an elastic net structure. *Ocean engineering*, 92:188–197, 2014.

[47] S Mandal and T Sahoo. Wave interaction with floating flexible circular cage system. In *Proceedings of the 11th International Conference on Hydrodynamics (ICHD 2014), Singapore*, pages 19–24, 2014.

[48] Wei Su, Jie-Min Zhan, and Hua Huang. Wave interactions with a porous and flexible cylindrical fish cage. *Procedia Engineering*, 126:254–259, 2015.

[49] Mingyuan Ma, Hong Zhang, Dong-Sheng Jeng, and Chien Ming Wang. A semi-analytical model for studying hydroelastic behaviour of a cylindrical net cage under wave action. *Journal of Marine Science and Engineering*, 9(12):1445, 2021.

[50] Konstantin Kokkinowrachos, Spyridon Mavrakos, and Sampson Asorakos. Behaviour of vertical bodies of revolution in waves. *Ocean Engineering*, 13(6):505–538, 1986.

[51] Abhijit Sarkar and Swaroop Nandan Bora. Hydrodynamic coefficients for a floating semi-porous compound cylinder in finite ocean depth. *Marine Systems & Ocean Technology*, 15(4):270–285, 2020.

[52] J Journée and W Massie. *Offshore Hydromechanics*. 01 2001.

[53] Klaus Hasselmann, Tim P Barnett, E Bouws, H Carlson, David E Cartwright, K Enke, JA Ewing, A Gienapp, DE Hasselmann, P Kruseman, et al. Measurements of wind-wave growth and swell decay during the joint north sea wave project (jonswap). *Ergaenzungsheft zur Deutschen Hydrographischen Zeitschrift, Reihe A*, 1973.

[54] Dimitrios Konispoliatis, Georgios Katsaounis, Dimitris Manolas, Takvor Soukissian, Stylianos Polyzos, Thomas Mazarakos, S. Voutsinas, and Spyridon Mavrakos. Refos: A renewable energy multi-purpose floating offshore system. *Energies*, 14:3126, 05 2021.